

Centroid moment tensor inversions of offshore earthquakes using a three-dimensional velocity structure model: slip distributions on the plate boundary along the Nankai Trough

Shunsuke Takemura¹, Ryo Okuwaki², Tatsuya Kubota³, Katsuhiko Shiomi³, Takeshi Kimura³ and Akemi Noda⁴

¹*Earthquake Research Institute, the University of Tokyo, 1-1-1 Yayoi, Bunkyo-ku, Tokyo 113-0032, Japan. E-mail: shunsuke@eri.u-tokyo.ac.jp*

²*Mountain Science Center, Faculty of Life and Environmental Sciences, University of Tsukuba, 1-1-1 Tennodai, Tsukuba 305-8572, Japan*

³*Network Center for Earthquake, Tsunami and Volcano, National Research Institute for Earth Science and Disaster Resilience, 3-1 Tennodai, Tsukuba, Ibaraki 305-0006, Japan*

⁴*Earthquake and Tsunami Research Division, National Research Institute for Earth Science and Disaster Resilience, 3-1 Tennodai, Tsukuba, Ibaraki 305-0006, Japan*

Accepted 2020 May 8. Received 2020 May 7; in original form 2019 November 17

SUMMARY

Due to complex 3-D heterogeneous structures, conventional 1-D analysis techniques using onshore seismograms can yield incorrect estimation of earthquake source parameters, especially dip angles and centroid depths of offshore earthquakes. Combining long-term onshore seismic observations and numerical simulations of seismic wave propagation in a 3-D model, we conducted centroid moment tensor (CMT) inversions of earthquakes along the Nankai Trough between April 2004 and August 2019 to evaluate decade-scale seismicity. Green's functions for CMT inversions of earthquakes with moment magnitudes of 4.3–6.5 were evaluated using finite-difference method simulations of seismic wave propagation in the regional 3-D velocity structure model. Significant differences of focal mechanisms and centroid depths between previous 1-D and our 3-D catalogues were found in the solutions of offshore earthquakes. By introducing the 3-D structures of the low-velocity accretionary prism and the Philippine Sea Plate, dip angles and centroid depths for offshore earthquakes were well-constrained. Teleseismic CMT also provides robust solutions, but our regional 3-D CMT could provide better constraints of dip angles. Our 3-D CMT catalogue and published slow earthquake catalogues depicted spatial distributions of slip behaviours on the plate boundary along the Nankai Trough. The regular and slow interplate earthquakes were separately distributed, with these distributions reflecting the heterogeneous distribution of effective strengths along the Nankai Trough plate boundary. By comparing the spatial distribution of seismic slip on the plate boundary with the slip-deficit rate distribution, regions with strong coupling were clearly identified.

Key words: Computational seismology; Earthquake ground motions; Earthquake source observations; Seismicity and tectonics; Wave propagation.

1 INTRODUCTION

Focal mechanisms of earthquakes and their spatial distributions are important for evaluating tectonic/local stress and strain fields (e.g. Townend & Zoback 2006; Terakawa & Matsu'ura 2010; Saito *et al.* 2018). To determine focal mechanisms, first-*P* or *S* polarization inversion (e.g. Hardebeck & Shearer 2002; Shelly *et al.* 2016) and waveform-based centroid moment tensor (CMT) inversion (e.g. Dziewonski *et al.* 1981; Kanamori & Rivera 2008; Ekström *et al.* 2012) techniques have been widely used around the world. 1-D earth models are assumed in typical focal mechanism

determination methods. In regions with complex 3-D heterogeneous structures, first-motion solutions using the 1-D earth model systematically show mis-estimations (e.g. Takemura *et al.* 2016). Although CMT methods based on long-period (> 10 s) waveforms can be applied only for moderate-to-large earthquakes due to signal-to-noise problems for long-period components, their evaluations of source parameters are generally robust against structural heterogeneities in comparison to first-motion solutions.

Along the Nankai Trough, megathrust earthquakes have repeatedly occurred at intervals of 100–150 yr (e.g. Ando 1975). Evaluating seismicity around this region is important for contributing

to the understanding of megathrust earthquakes, such as evaluating stress accumulation/release processes on plate boundaries. In Japan, regular and slow earthquakes have been systematically monitored by the seismic networks of the Monitoring of Waves on Land and Seafloor (MOWLAS; <https://doi.org/10.17598/NIED.0009>) operated by the National Research Institute for Earth Science and Disaster Resilience (NIED; Okada *et al.* 2004). According to the combined earthquake catalogues of the International Seismological Centre-Global Earthquake Model (ISC-GEM; Storchak *et al.* 2013), the Japan Meteorological Agency (JMA), and the NIED F-net (Fukuyama *et al.* 1998; Kubo *et al.* 2002), the seismicity of regular earthquakes along the Nankai Trough, especially interplate earthquakes, is quite low. Fig. 1 shows the spatial distribution of regular earthquakes with moment magnitudes (M_w) of 4.3–6.5 that occurred from April 2004 to August 2019, as listed in the F-net moment tensor (F-net MT) catalogue. The regional moment tensor inversion can be applied to earthquakes with $M_w >$ about 4, which is smaller than a lower limit of teleseismic moment tensor inversion (e.g. Fig. 5 of Ekström *et al.* 2012). This is an advantage for discussing detail seismicity in a certain region. A few shallow offshore earthquakes occurred in the Tonankai and Nankai regions, and their focal mechanisms in the F-net catalogue were not characterised by low-angle thrust faulting. In other words, no earthquakes suggesting faulting on the plate boundary around the Tonankai and Nankai regions are listed in the F-net MT catalogue.

On 1 April 2016, the M_w 5.8 earthquake, called ‘2016 southeast off the Kii Peninsula earthquake’, occurred in the Tonankai region (marked A in Fig. 1). The F-net MT solution of this earthquake was characterised by high-angle (38°) reverse faulting below the upper surface of the Philippine Sea Plate, indicating it was an intraslab earthquake. However, a detailed analysis of this earthquake revealed that it could be modelled by low-angle thrust faulting at a depth of approximately 10 km, suggesting seismic slip along the plate boundary (e.g. Wallace *et al.* 2016; Nakano *et al.* 2018a; Takemura *et al.* 2018a). Source models suggested in these studies were also consistent with a model based on observed tsunami data (Kubota *et al.* 2018). In regions with a thick accretionary prism, characteristics of surface wave propagation are significantly affected by a low-velocity accretionary prism (e.g. Shapiro *et al.* 1998; Gombert 2018; Kaneko *et al.* 2019). Thus, the focal mechanisms of other offshore earthquakes along the Nankai Trough could be incorrectly estimated using conventional 1-D regional MT inversion, even for long-period displacements. Indeed, shallow very low frequency earthquakes along the Nankai Trough have been interpreted as low-angle thrust faulting on the plate boundary by using offshore seismic observations (e.g. Nakano *et al.* 2018), but their focal mechanisms based on 1-D analysis of onshore observations were high-angle reverse faulting mechanisms within the accretionary prism (e.g. Ito & Obara 2006). To evaluate seismic activity along the Nankai Trough more precisely, offshore earthquakes listed in the previous 1-D catalogues require re-analysis.

Parallel simulation codes of seismic wave propagation (e.g. Gokhberg & Fichtner 2016; Maeda *et al.* 2017) and 3-D seismic velocity structure models (e.g. Eberhart-Phillips *et al.* 2010; Koketsu *et al.* 2012) enable the simulation of Green’s functions propagating through realistic 3-D earth models (hereafter called ‘3-D Green’s functions’), which have been used to develop CMT inversions (e.g. Ramos-Martínez & McMechan 2001; Lee *et al.* 2013; Hejrani *et al.* 2017; Okamoto *et al.* 2018; Takemura *et al.* 2018a,b, 2019a,b,c, Wang & Zhan 2020). Although the resolution of detailed source characteristics for offshore earthquakes derived using the 3-D CMT method and onshore seismograms is limited compared to those

using offshore observations, these methods provide similar focal mechanisms and centroid locations (see fig. 2 of Takemura *et al.* 2018b). Thus, offshore seismic activity, including earthquakes before offshore seismic observations, can be effectively evaluated.

To investigate the decade-scale seismicity of offshore earthquakes along the Nankai Trough, we re-evaluated focal mechanisms based on CMT inversion using 3-D Green’s function data sets, which were evaluated by numerical simulations of seismic wave propagation in a regional 3-D velocity structure model. Then, to investigate spatial variation in slip behaviours on the plate boundary along the Nankai Trough, we compared the spatial distribution of focal mechanisms based on the 3-D CMT technique with the spatial distribution of slip-deficit rates (Noda *et al.* 2018), slow slip events (SSEs; Miyazaki *et al.* 2006; Nishimura *et al.* 2013; Kobayashi 2014; Takagi *et al.*, 2016, 2019; Yokota & Ishikawa 2020), shallow low-frequency tremors (LFTs; Yamashita *et al.* 2015), shallow very low-frequency earthquakes (VLFES; Takemura *et al.* 2019b) and the 1968 Hyuga-nada earthquake (Yagi *et al.* 1998).

2 DATA AND METHODS

We used three-component (NS, EW and UD) velocity seismograms from F-net (NIED 2019), for which the performance of the sensors have been systematically monitored (Kimura *et al.* 2015). To conduct CMT inversion of the target earthquakes, we applied a bandpass filter with passed periods of 25–100 s. We selected a 25–100 s period band because ground motions for periods of 8–20 s are significantly affected by internal structures of the accretionary prism along the Nankai Trough (e.g. Takemura *et al.* 2019a). The selected period band is enough longer than corner periods of source spectra for target earthquakes. In our CMT inversions, we used 10-min F-net velocity seismograms from three minutes before the initial origin minute to conduct pre-processing (filter and integration) stably. We obtained displacement waveforms by calculating time integration of each filtered velocity record. The target earthquakes occurred within the region of assumed source grids (grey crosses in Fig. 2) between April 2004 and August 2019, and values of M_w in the F-net catalogue ranging from 4.3 to 6.5. According to the signal-to-noise ratios for the target period band, the magnitude range of the analysed earthquake was determined by trial and error. Source grids were uniformly distributed at horizontal intervals of 0.1° . Depths of source grids ranged from 6 to 50 km at an interval of 2 km. The total number of source grids was 61 433.

Green’s functions were evaluated by solving equations of motion in the 3-D viscoelastic medium model based on the finite-difference method (FDM) simulations. The 3-D simulation model covered an area of $900 \times 1000 \times 100 \text{ km}^3$, which was discretized by grid intervals of 0.5 km in the horizontal direction and 0.2 km in the vertical direction. We used a parallel simulation code of OpenSWPC (Maeda *et al.* 2017), which includes the reciprocal calculation mode for effectively evaluating Green’s functions. The reciprocal calculation has proved very useful in the case that the number of seismic source grids is significantly larger than the number of seismic stations (e.g. Eisner & Clayton 2001; Hejrani *et al.* 2017; Okamoto *et al.* 2018). We obtained a total of approximately 35 000 000 Green’s function SAC files from 61 433 source grids to 32 F-net stations (black and blue filled triangles in Fig. 2) via 96 reciprocal FDM calculations. The source time function of each Green’s function was the Küpper wavelet with a duration of 1 s.

The 3-D velocity model of Koketsu *et al.* (2012) was used, as it has been widely applied in studies of seismic ground motions across

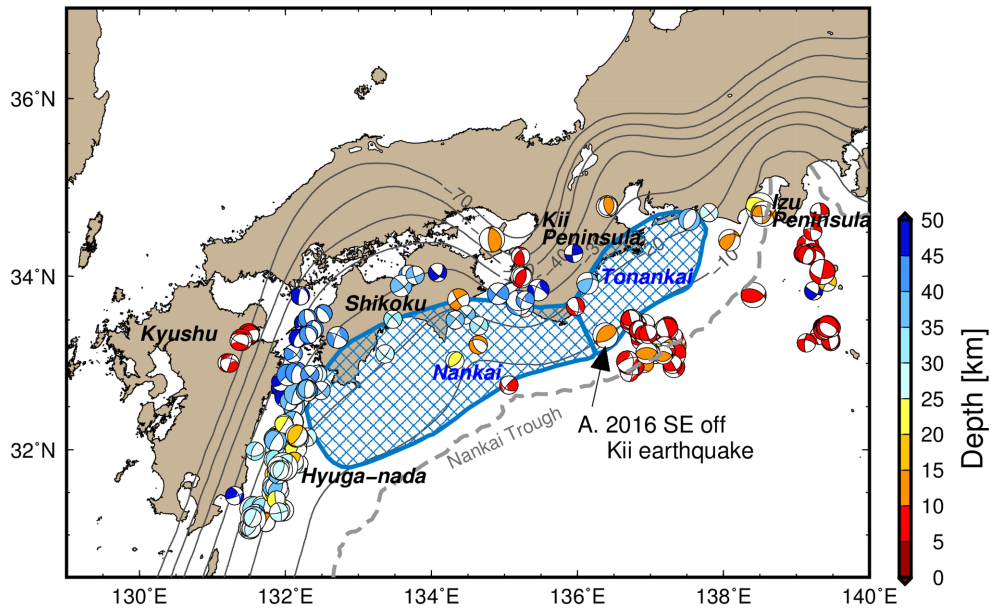


Figure 1. Map of the study region. The black contour lines are the iso-depth contour lines of the upper surface of the Philippine Sea Plate of Koketsu *et al.* (2012). Focal mechanisms are the moment tensor (MT) solutions of regular earthquakes with M_w of 4.3–6.5 in the F-net catalogue (Fukuyama *et al.* 1998, Kubo *et al.* 2002) that occurred in the area with latitudes less than 34.8°N , longitudes greater than 131°E , and at depths of less than 50 km. The plotted MT solutions range from April 2004 to August 2019. The blue hatched areas represent the expected source region of the Nankai and Tonankai earthquakes (available at: http://www.jishin.go.jp/main/chousa/01sep_nankai/index.htm). The earthquake marked A is the M_w 5.8 southeast off Kii Peninsula earthquake that occurred on 1 April 2016.

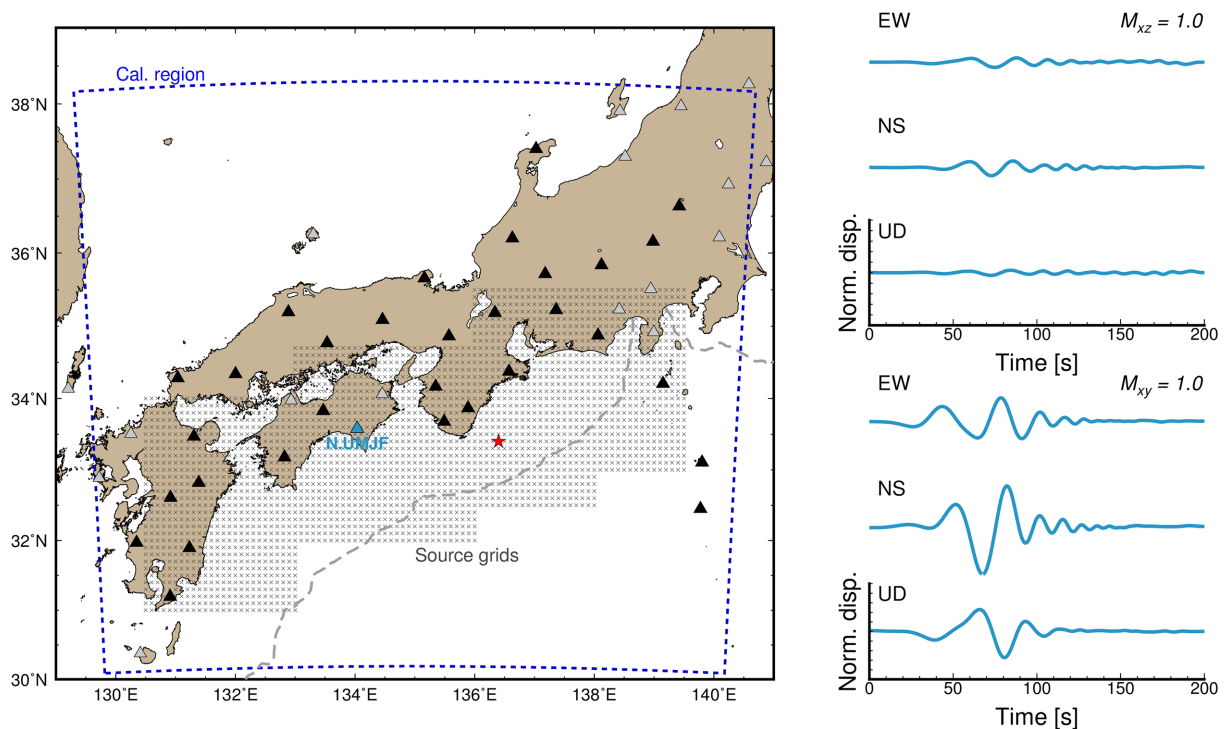


Figure 2. Calculation settings used in this study were the blue dashed line represents the horizontal coverage of the simulation model region. The triangles and crosses in the map denote the locations of the F-net stations and the assumed source grids, respectively. Green's functions from the source grids to the black-fill and blue-fill triangles were evaluated via reciprocal calculations using OpenSWPC code (Maeda *et al.* 2017). The right-hand panels show examples of filtered displacement Green's functions from a certain hypocentre (red star, at a depth of 10 km) to the N.UMJF station (blue triangle), whose epicentral distance is 263 km. The filter passband was 25–100 s.

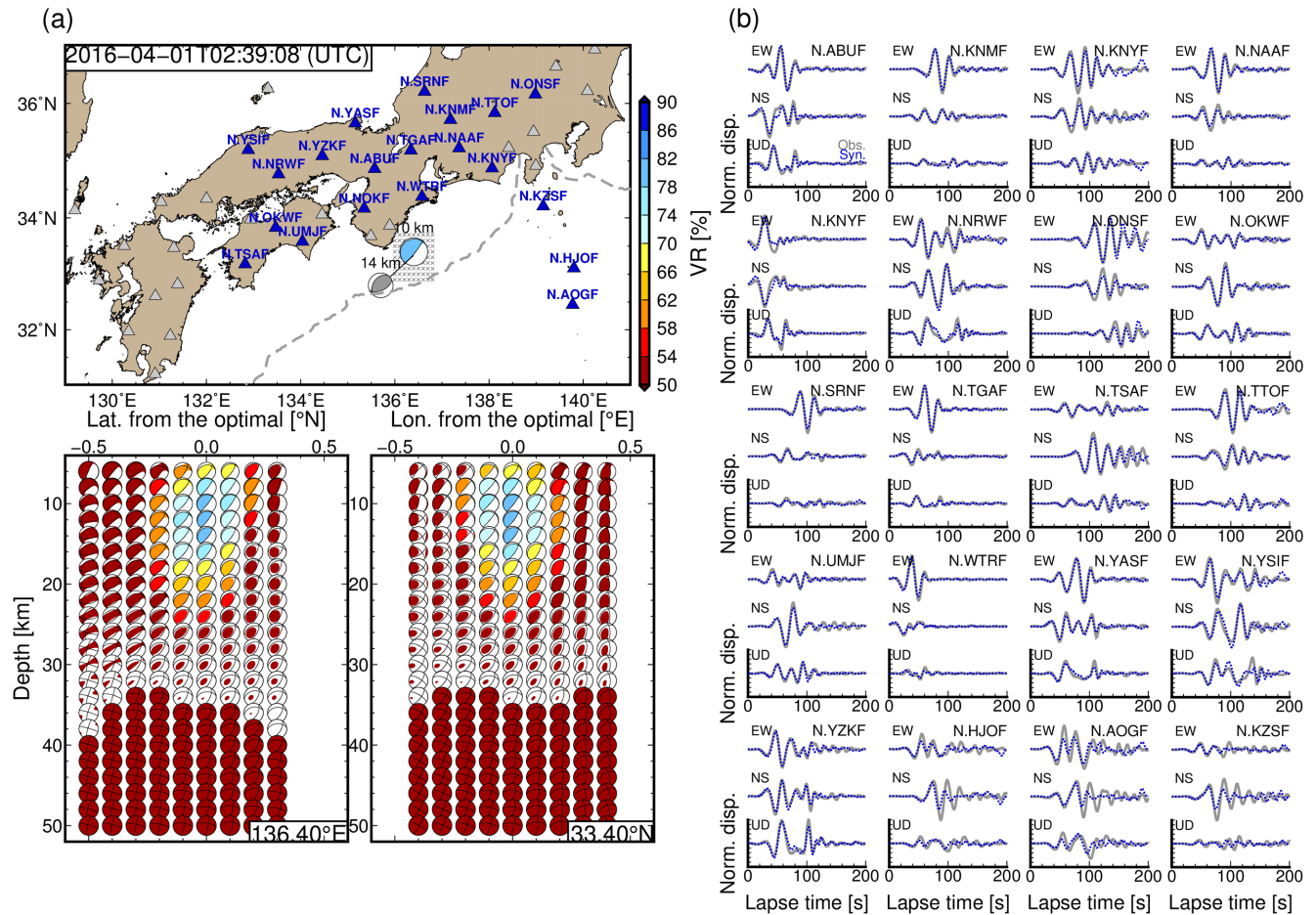


Figure 3. CMT results for the southeast off Kii Peninsula earthquake that occurred on 1 April 2016. (a) Locations of the optimal solutions, used stations and depth variations of optimal solutions at each source grid. Colours of the focal mechanisms reflect values of variance reduction between observed and synthetic displacements in the 25–100 s period band. The numbers above the optimal solutions in (a) are the optimal centroid depths. The grey focal mechanism in (a) is the F-net MT solution of this earthquake. (b) Comparisons of observed and synthetic displacements in the 25–100 s period band. Grey solid and blue dotted lines are the observed and synthetic seismograms, respectively. Synthetic seismograms were evaluated by assuming the optimal solution. Amplitudes at each station were normalized by the maximum amplitude of both observed and synthetic three-component displacement waveforms. Detailed source parameters are listed in Table S1.

Japan. The configurations of the subducting oceanic plate and the Moho discontinuity are consistent with other models (e.g. Shiomi *et al.* 2006; Hirose *et al.* 2008). The oceanic crust of the model of Koketsu *et al.* (2012) has approximately 7 km thickness, which corresponds to those by seismic surveys (e.g. Nakanishi *et al.* 2002). The topography model in our simulations was the ETOPO1 model (Amante & Eakins 2009). The P - and S -wave velocities and density (V_P , V_S and ρ) in the seawater layer were 1.5 km s⁻¹, 0.0 km s⁻¹ and 1.04 g cm⁻³, respectively. The air column was modelled as a vacuum with V_P of 0.0 km s⁻¹, V_S of 0.0 km s⁻¹ and ρ of 0.001 g cm⁻³. The minimum V_S in the solid column of 1.5 km s⁻¹ was assumed. The accretionary prism is important for constraining centroid depth, but detail velocity structure within the accretionary prism has limited effects on long-period (> 20 s) seismograms (figs 5 and 6 of Takemura *et al.* 2019a).

Simulations were conducted using the computer system of the Earthquake and Volcano Information Center at the Earthquake Research Institute, the University of Tokyo. Each simulation required 385 GBytes of computer memory and a wall-clock time of 2.5 hr and was performed using parallel computing with 432 cores to evaluate seismic wave propagation of 200 s with 20 000 time-step

calculations. According to our grid and model settings, our FDM simulation can precisely evaluate long-period (> 10 s) seismic wave propagation.

Examples of Green's functions are illustrated in the right-hand panels of Fig. 2. The source (red star) was located at a depth of 10 km, near the plate boundary. We used the Cartesian coordinate system of Aki & Richards (2002), where x , y and z are taken as north, east and down, respectively. Due to the low-velocity accretionary prism and seawater, durations of surface waves were amplified and elongated. In particular, for $M_{xy} = 1.0$ (i.e. a pure strike-slip with strike angle of 0°, dip angle of 90° and rake angle of 0°), Love waves on horizontal components were strong and long. We assumed six-element moment tensors for the CMT inversions, which includes five double couple and isotropic moment tensors (e.g. Kikuchi & Kanamori 1991).

In the CMT inversions, we basically used Green's functions at F-net stations within epicentral distances of 100–400 km from the initial epicentre. The initial epicentre was obtained from the F-net MT catalogue. In cases where earthquake $M_w < 4.5$, we selected a distance range of 100–350 km due to the signal-to-noise ratio of the observed waveforms for the analysed period. We visually checked

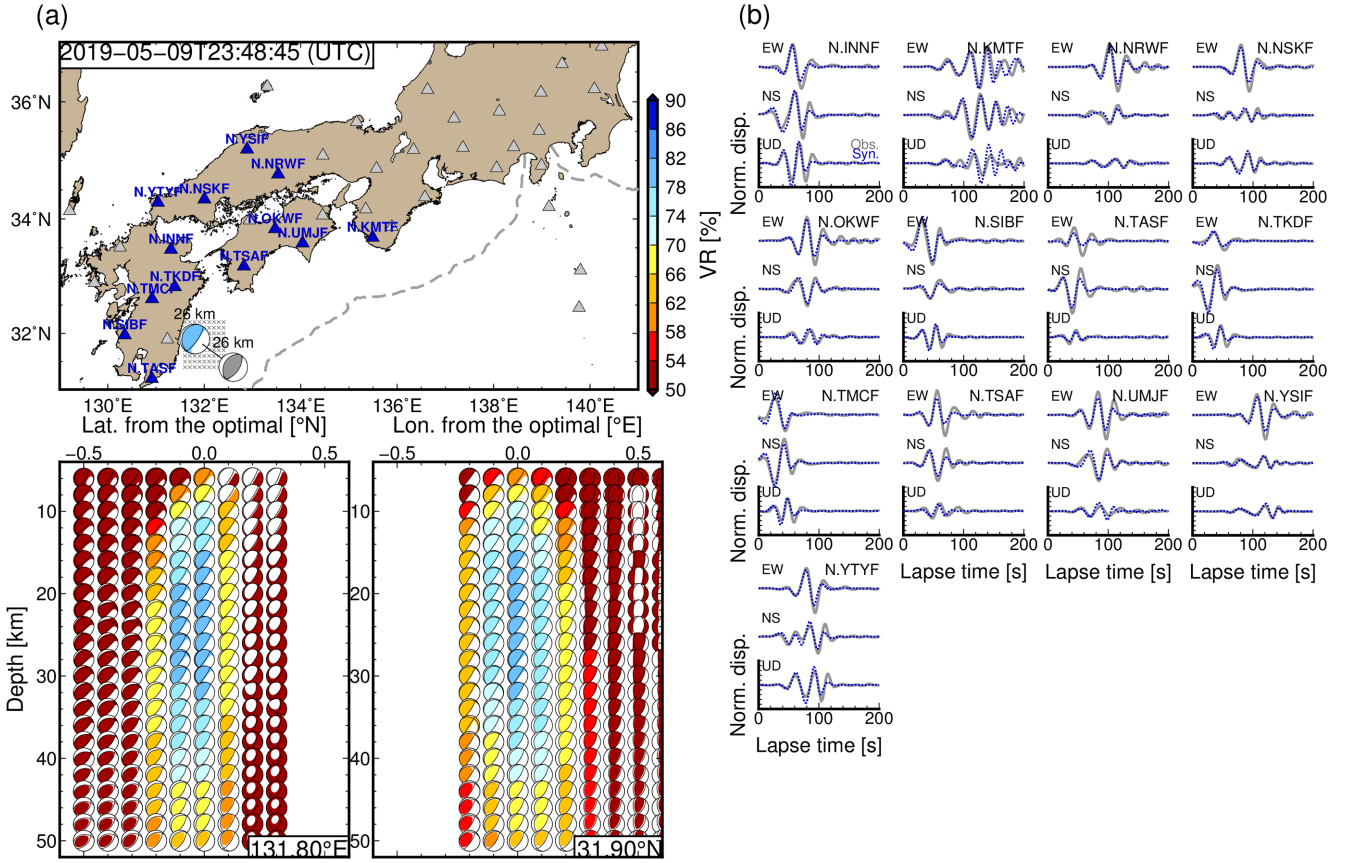


Figure 4. CMT results for the Hyuga-nada earthquake that occurred on 9 May 2019. (a) Locations of the optimal solutions, used stations, and depth variations of optimal solutions at each source grid. Colours of the focal mechanisms reflect values of variance reduction between observed and synthetic displacements in the 25–100 s period band. The numbers above the optimal solutions in (a) are the optimal centroid depths. The grey focal mechanism in (a) is the F-net MT solution of this earthquake. (b) Comparisons of observed and synthetic displacements in the 25–100 s period band. Grey solid and blue dotted lines are the observed and synthetic seismograms, respectively. Synthetic seismograms were evaluated by assuming the optimal solution. Amplitudes at each station were normalized by the maximum amplitude of both observed and synthetic three-component displacement waveforms. Detailed source parameters are listed in Table S1.

the filtered displacement waveforms and discarded noisy ones. Centroid location and time of the analysed earthquake were determined using grid search inversion. Because the analysis period range was longer than the source durations of target earthquakes with $M_w = 4.3$ – 6.5 , we did not estimate source durations of these events. A set of Green's functions at the source grids, which were located in a $\pm 0.4^\circ$ region from the initial epicentre and were distributed at depths of 6–50 km, was selected for the grid search inversion.

The CMT inversions were conducted for each selected source grid every 1 s from three minutes before the origin minute as recorded in the F-net catalogue. We used a 200-s time window for each CMT inversion. During grid search CMT inversion, we did not allow time shifts between synthetic and observed seismograms. After CMT inversion at all of the selected source grids, we obtained seismic moments and focal mechanisms at all locations and times. To identify the optimal solution, we evaluated variance reductions (VRs) between the observed and synthetic displacement seismograms for periods of 25–100 s. The VR could then be evaluated using the following equation:

$$VR = \left[1 - \frac{\sum_{i=1}^{N_S} \int (u_i^{Obs.}(t) - u_i^{Syn.}(t))^2 dt}{\sum_{i=1}^{N_S} \int (u_i^{Obs.}(t))^2 dt} \right] \times 100 \text{ [per cent]}, \quad (1)$$

where N_S is the number of stations and $u_i^{Obs.}$ and $u_i^{Syn.}$ are the time-series of observed and synthetic displacements, respectively. If observed and synthetic seismograms are perfectly matched, VR is 100 per cent. The solution with the maximum VR was considered the optimal solution, providing the optimal centroid location, depth, time, focal mechanism and seismic moment of each earthquake. In the case that the optimal solution was located at the edges of the initial source grids, we performed the CMT inversion again using Green's functions for a broader source grid data set. In the cases of regions around the edges of all source grids (all crosses in Fig. 2), such as southern Kyushu and eastern Izu, we could not extend the grid set, and then the optimal solution was located at the grid edge. These events may include possibilities of some shifts outside the edges of the assumed source grids. Our grid search CMT inversion required approximately 15–20 min using a typical, single-core desktop machine.

3 RESULTS

We obtained a total of 215 CMT solutions for moderate earthquakes that occurred between April 2004 and August 2019. We discarded the solutions with a maximum VR of less than 20 per cent. Our 3-D CMT catalogue is listed in Global CMT (GCMT) format in the Supplementary data (Table S1) and the CSV format full catalogue

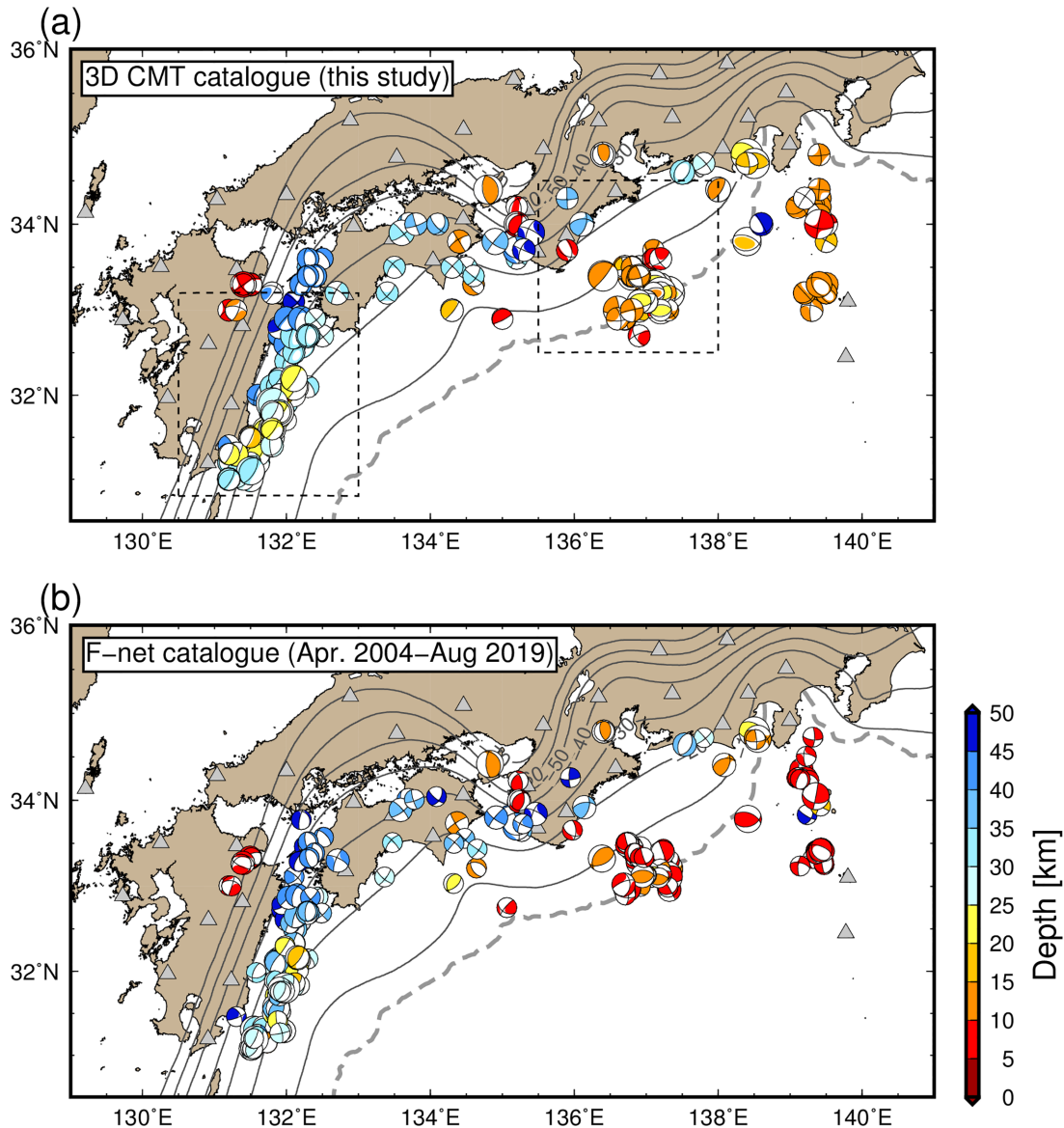


Figure 5. Comparisons of estimated CMT solutions between the (a) 3-D CMT and (b) F-net MT catalogues. Colours of focal mechanisms represent the centroid depths of each solution. Detailed source parameters of our 3-D CMT solutions are listed in Table S1. The regions enclosed by the dashed lines in (a) are enlarged in Figs 6 and 7.

data is available from <https://doi.org/10.5281/zenodo.3674161>. The size distribution and magnitude–time diagram of our 3-D CMT catalogue are shown in Figs S1 and S2. The estimated moment magnitudes were slightly changed from the original F-net catalogue. The VRs of earthquakes with small magnitudes tended to be low (Fig. S2) due to the signal-to-noise ratio for the analysed period range. We also compared our results with the GCMT catalogue (Fig. S1). Teleseismic CMT inversion is robust, but our regional CMT catalogue contains more earthquakes, whose M_w values are less than about 5.

Figs 3 and 4 show examples of CMT solutions for the southeast off the Kii Peninsula earthquake (1 April 2016) and the Hyuganada earthquake (9 May 2019), respectively. In our previous study (Takemura *et al.* 2018a), the 2016 southeast off the Kii Peninsula earthquake was also analysed. The epicentre location and origin

time were fixed in the previous study. We re-analysed this earthquake via full 3-D CMT inversion, which estimates centroid location, depth, time and moment tensor. The F-net MT solution of this earthquake was a high-angle (38°) reverse faulting mechanism (grey focal sphere in Fig. 3). Its optimal solution is an M_w 5.9 low-angle (10°) thrust faulting at a depth of 10 km (Fig. 3), which is close to the plate boundary (e.g. Park *et al.* 2010; Kamei *et al.* 2012). The synthetic seismograms of the optimal solution corresponded well with the observations. The depth variation of VRs illustrated a clear peak around the optimal depth. The centroid depth of this earthquake was well constrained by our CMT inversion. Takemura *et al.* (2018a) numerically demonstrated that the low-velocity accretionary prism just above the seismic source—which controls long-period surface wave propagation—provides a better constraint on the centroid depth. They also demonstrated that the 3-D oceanic

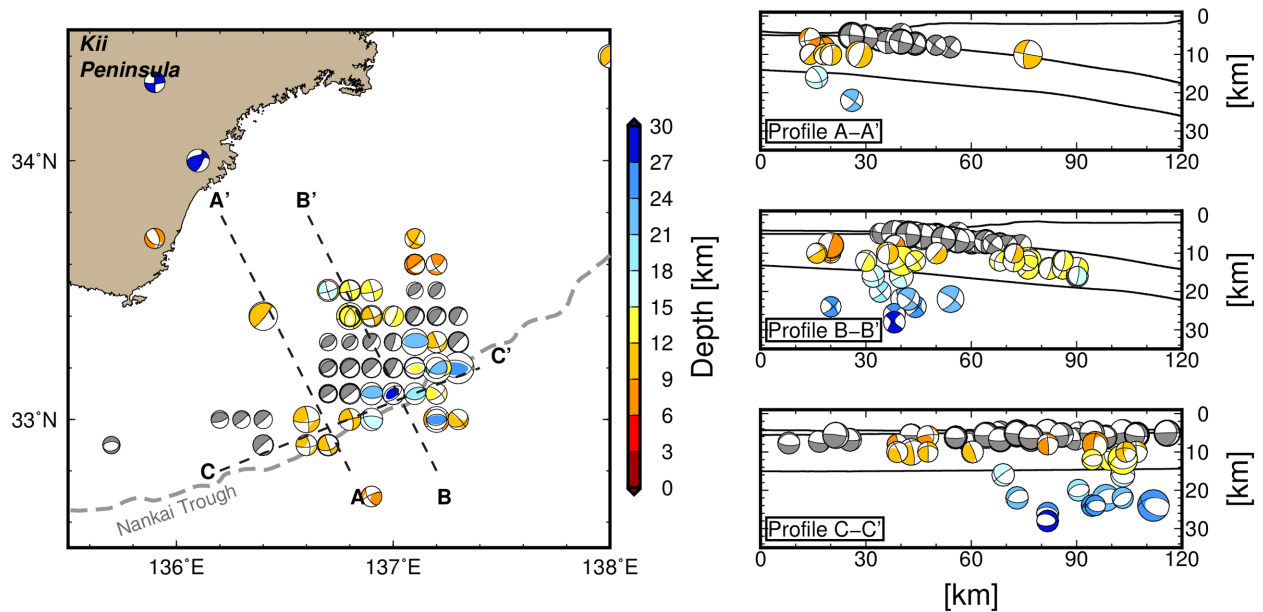


Figure 6. Spatial distribution of the CMT solutions southeast of the Kii Peninsula. Coloured focal mechanisms are our CMT solutions. Grey focal mechanisms are the CMT solutions of shallow VLFs (Takemura *et al.* 2019b). The right-hand panels show cross-sections along profiles A–A', B–B' and C–C'. The bathymetry of ETOPO1 (Amante & Eakins 2009), the upper surface, and oceanic Moho of the Philippine Sea Plate (Koketsu *et al.* 2012) along each profile are plotted in the right-hand panels.

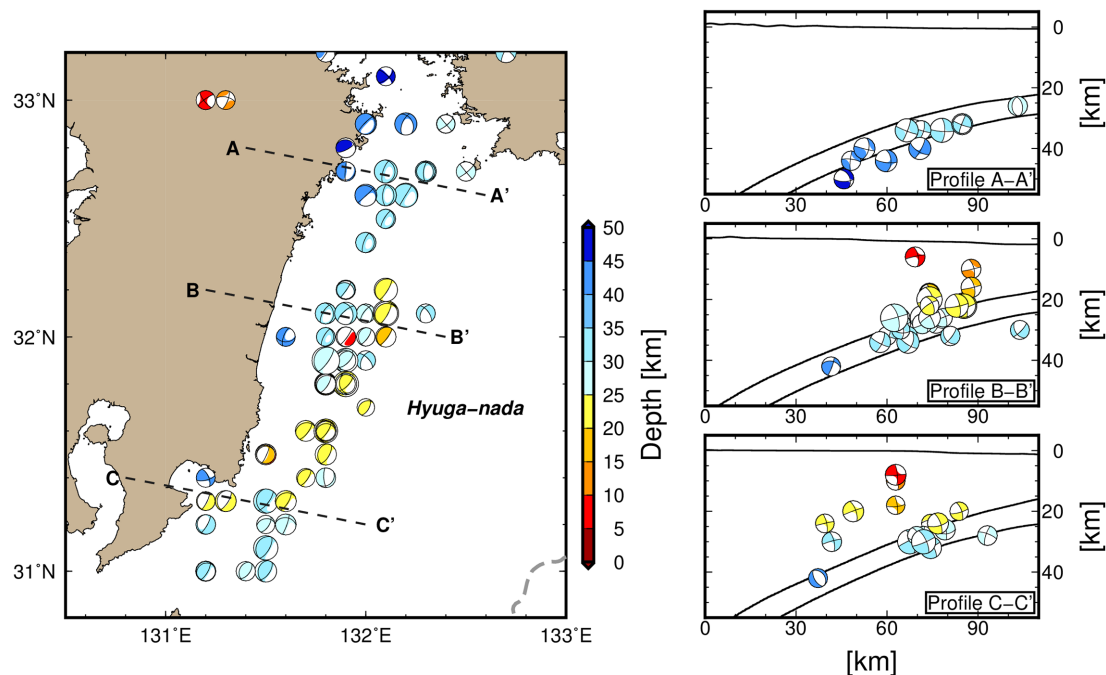


Figure 7. CMT results for the Hyuga-nada region. Coloured focal mechanisms are our CMT solutions. The right-hand panels show cross-sections along profiles A–A', B–B' and C–C'. The bathymetry of ETOPO1 (Amante & Eakins 2009), the upper surface, and oceanic Moho of the Philippine Sea Plate (Koketsu *et al.* 2012) along each profile are plotted in the right-hand panels.

plate has an important role in constraining focal mechanism (figs 7 and 8 of Takemura *et al.* 2018a).

The centroid location was also close to that estimated by ocean-bottom seismometers deployed just above the source region (Wallace *et al.* 2016; Nakano *et al.* 2018a), while the GCMT solution was slightly (0.2°) shifted to the south (Fig. S3). The CMT result was consistent with models estimated by offshore observations

(Wallace *et al.* 2016; Kubota *et al.* 2018; Nakano *et al.* 2018a). Especially, by using traveltimes, tsunami and afterslip records, Wallace *et al.* (2016) and Nakano *et al.* (2018a) concluded that this earthquake could be interpreted as an interplate earthquake. Our CMT solution based on 3-D Green's functions and onshore seismograms also suggests this earthquake was due to faulting on the plate boundary.

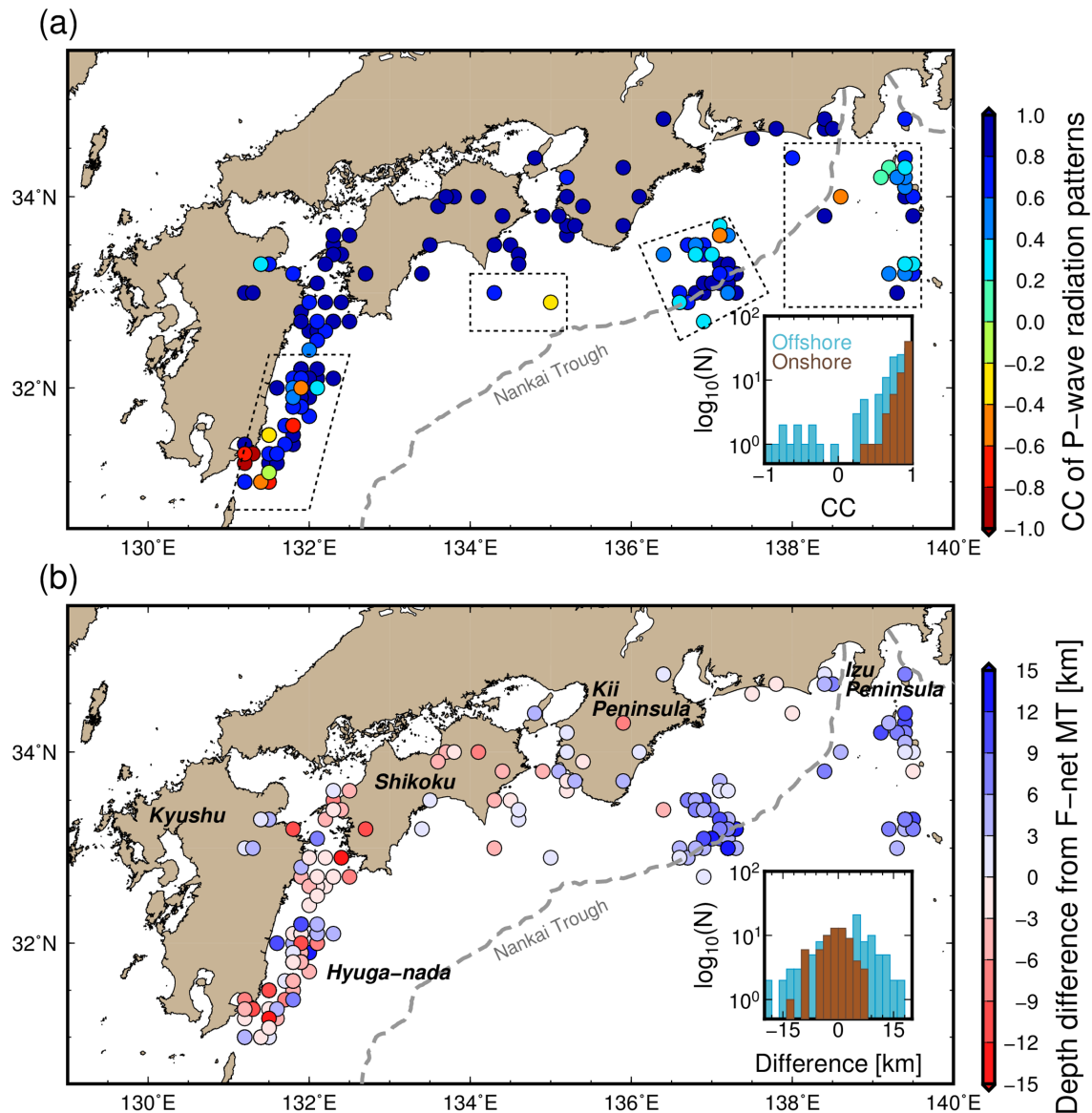


Figure 8. Spatial distributions of (a) correlation coefficients (CCs) of P -wave radiation patterns between 3-D CMT and F-net solutions and (b) depth differences of 3-D CMT solutions from the F-net catalogue. Lower right panels in (a) and (b) show histograms of CCs and differences, respectively. Offshore earthquakes are defined as earthquakes that occurred within regions closed by dotted lines in (a).

Fig. 4 shows the results of the CMT inversion and waveform fitting for the Hyuga-nada earthquake on 9 May 2019. The F-net MT solution was also high-angle (33°) reverse faulting. The optimal CMT solution indicated an M_w 6.2 low-angle (16°) thrust mechanism. The dip angle from the CMT solution agreed well with that of the Philippine Sea Plate around this earthquake. The synthetic waveforms also corresponded well to observed ones. Although the optimal depth (26 km) was determined to be close to the upper surface of the Philippine Sea Plate (approximately 27 km), a high VR (>80 per cent) area was found within a wider depth range (16–32 km). Because the depth of this earthquake was deeper than the 2016 southeast off the Kii Peninsula earthquake, the effects of the low-velocity accretionary prism might not have been so strong. Thus, the depth resolution of the CMT solutions might not be good when compared to the case of the 2016 southeast off the Kii Peninsula earthquake. To constrain the hypocentre depth more sharply, additional data, such as shorter-period

(~ 4 s) first-arrival P -wave waveforms, would need to be considered (e.g. Okamoto *et al.* 2018; Takemura *et al.* 2018a; Wang & Zhan 2020).

Fig. 5 shows a comparison of the estimated focal mechanisms for the F-net and our 3-D CMT catalogues. Our CMT solutions of onshore earthquakes did not differ significantly from the F-net solutions. However, our offshore CMT solutions differ from those based on the F-net 1D analysis. In particular, dip angles and centroid depths of offshore earthquakes—which are important for distinguishing interplate and intraslab earthquakes—were different. Differences in dip angles and depths were clearly illustrated in detailed comparisons of seismicity southeast off the Kii Peninsula and the Hyuga-nada (Figs 6, 7, S4 and S5). The conventional 1-D CMT inversion poorly estimated the dip angles of offshore earthquakes that occurred outside of onshore seismic arrays due to the lack of the 3-D subducting oceanic plate and the accretionary prism (e.g. Takemura *et al.* 2018a,b). The comparisons and error estimations

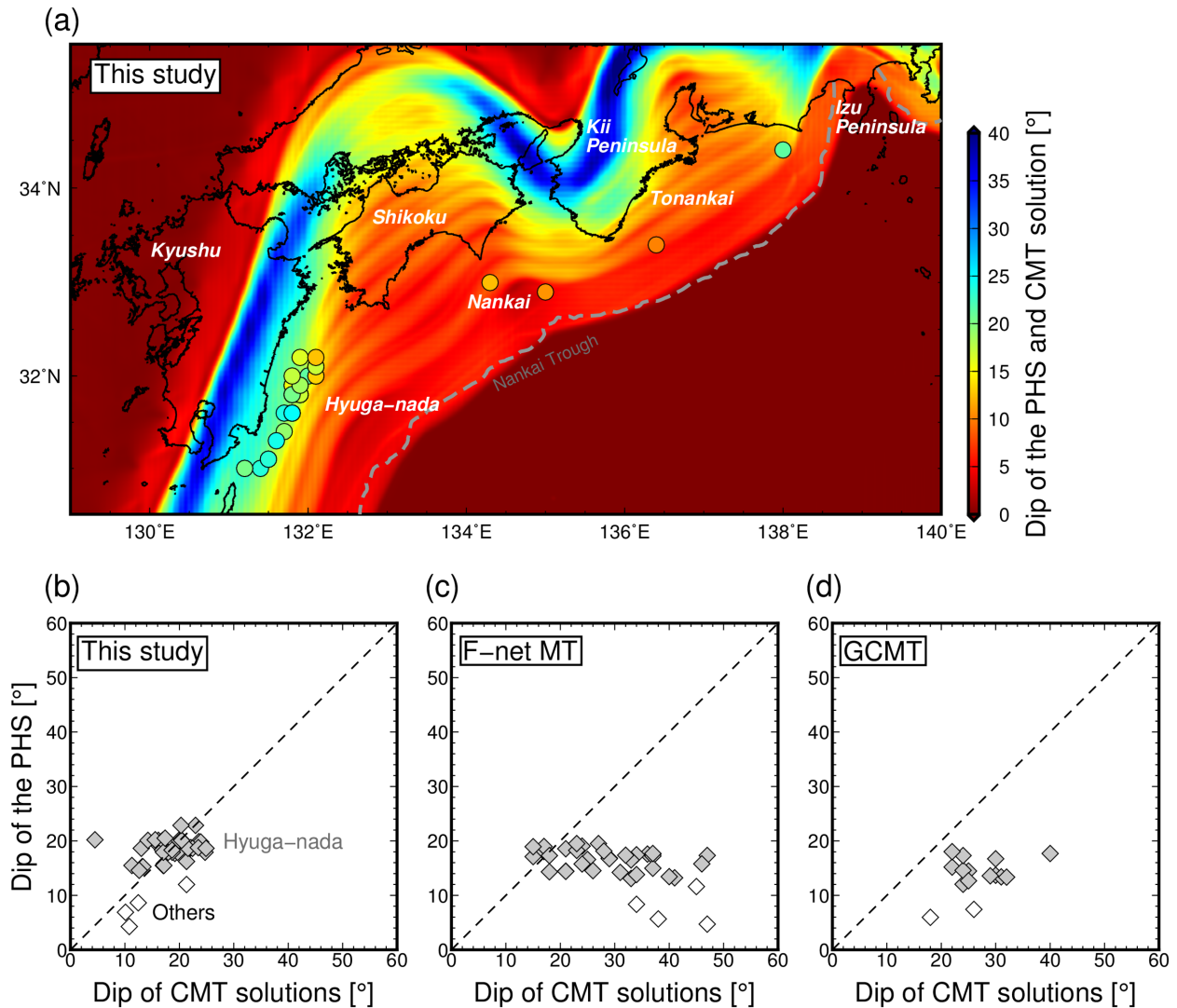


Figure 9. Comparisons of dip angles between the Philippine Sea Plate (PHS) and CMT solutions for suggestive interplate earthquakes. (a) Map of the region, comparisons of dip angles of the Philippine Sea Plate with (b) CMT solutions of this study and (c) F-net MT solutions. The background colour in (a) represents the spatial distribution of dip angles of the Philippine Sea Plate. The coloured circles denote dip angles of CMT solutions in this study. We compared dip angles between the Philippine Sea Plate and (c) F-net MT and (d) GCMT solutions of corresponding earthquakes.

of dip angles are shown in Figs 9 and 10. The comparison of spatial distributions of CMT solutions with the GCMT catalogue is also shown in Fig. S3.

We focused our attention on seismicity southeast off the Kii Peninsula and the Hyuga-nada (local names are shown in Fig. 1), where seismic activities are relatively high in the Nankai subduction zone. Fig. 6 shows spatial distributions of the CMT solutions southeast off the Kii Peninsula. We also plotted shallow VLFs in the catalogue of Takemura *et al.* (2019b) as grey focal spheres. Shallow VLFs, which were characterised by low-angle thrust faulting, were concentrated near the trench. In the region with shallow VLF active, low-angle thrust type CMT solution at depths of 5–10 km, which suggests seismic slip on the plate boundary, was not estimated. On the downdip side of the shallow VLF region, a low-angle thrust faulting mechanism was estimated at a depth near the plate boundary (along with profile A in Fig. 6). This earthquake is the 2016 southeast off the Kii Peninsula earthquake (Fig. 3). Almost all of the other earthquakes plotted in Fig. 6 are aftershocks of

the 2004 M_w 7.5 intraslab earthquake that occurred on 5 September 2004 southeast off the Kii Peninsula. Our CMT solutions of these aftershocks were separately distributed at two depths within the oceanic crust and mantle (10–15 and 20–30 km depths). This separation corresponded well to the hypocentre depth distributions of the aftershocks of the M_w 7.5 earthquake as determined using ocean-bottom seismometers (e.g. Sakai *et al.* 2005; Nakano *et al.* 2015). On the other hand, almost all the centroid depths of the F-net solutions were concentrated within the accretionary prism, crust and oceanic crust (5–15 km depths; Fig. S3). According to comparisons with the detail hypocentre distributions in this region, even for earthquakes near the trough axis, our CMT method provided better constraints for centroid depths, compared to the 1-D F-net MT solutions.

Fig. 7 shows the spatial distribution of CMT solutions around the Hyuga-nada region. Our CMT solutions characterized by low-angle thrust faulting mechanisms were distributed across the region with average slip rates of approximately 20–40 mm yr⁻¹ as

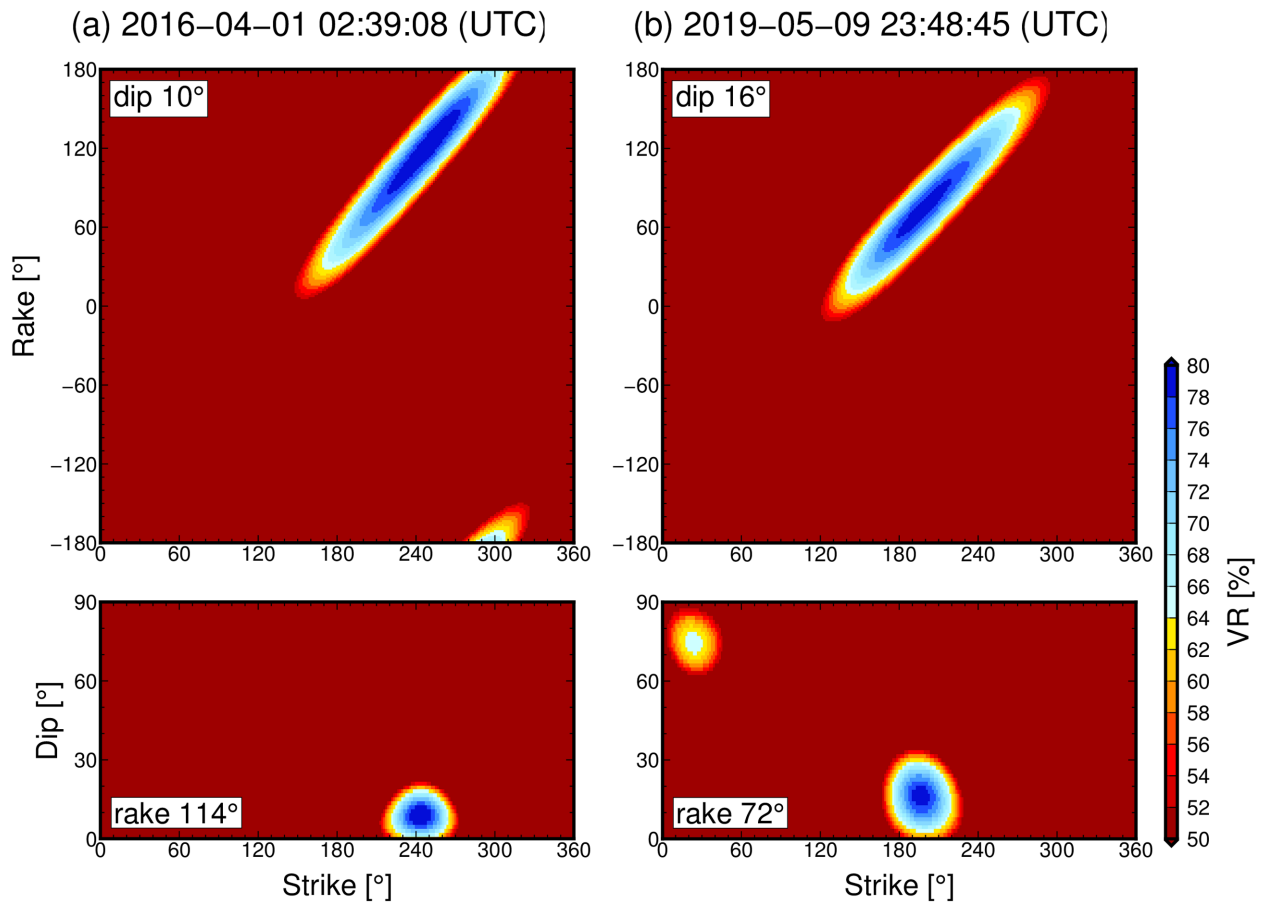


Figure 10. Distributions of variance reductions (VR) in the strike-rake and strike-dip planes for (a) the southeast off Kii Peninsula earthquake on 1 April 2016 and (b) the Hyuga-nada earthquake on 9 May 2019. In synthetics of displacement seismograms with various strike, dip, and rake, we assumed pure double-couple point sources and fixed hypocentre locations and seismic moments from CMT results (Figs 3 and 4).

inferred from small repeating earthquakes (e.g. Yamashita *et al.* 2012). The optimal centroid depths of such thrust solutions were concentrated around the plate boundary (profiles B and C in Fig. 7). The distribution of our CMT solutions agreed with that derived from onshore and temporal offshore seismometers (Tahara *et al.* 2008). The 3-D CMT solutions, especially for depths and low-angle thrust faulting mechanisms, corresponded to the areas of detected repeating earthquakes (Yamashita *et al.* 2012). Our 3-D CMT also worked well in this region. The dip angles of the F-net MT solutions at depths around the plate boundary were slightly higher than those of the plate boundary, as shown in Fig. S4. The centroid depths of the F-net catalogue were also slightly deeper than the depths of the plate boundary. These also might have been due to a lack of 3-D geometry of the subducting oceanic plate in the 1-D analysis.

To evaluate differences between 3-D CMT and F-net MT solutions, we calculated correlation coefficients of *P*-wave radiation patterns (e.g. Kuge & Kawakatsu 1993; Helffrich 1997) between two catalogues. We also calculated differences of estimated centroid depths from corresponding F-net solutions. Fig. 8 shows the spatial distribution of correlation coefficients of *P*-wave radiation patterns and depth differences between our CMT and F-net MT catalogues. The values of correlation coefficients of offshore earthquakes (enclosed by dashed lines in Fig. 8a) were widely distributed. Centroid depths of offshore earthquakes were also different from those of the F-net catalogue. Other earthquakes, which occurred

in onshore regions or had good station coverages, have high similarities and small depth differences. The rigidity of the 3-D model complicatedly depends on the centroid location, and consequently, depth shifts could cause shifts of moment magnitudes from the F-net catalogue (Fig. S1). We also plotted comparisons of estimated depths with corresponding GCMT solutions in Fig. 3(c). Almost of our centroid depths were 0–5 km shallower than those in the GCMT catalogue.

The parameter of the dip angle is important for distinguishing earthquake types. In the Nankai subduction zone, because megathrust earthquakes have repeatedly occurred, seismicity of interplate earthquakes is important. We selected low-angle thrust faulting solutions at depths around the plate boundary from our 3-D CMT catalogue. These selected events could be interpreted as seismic slips on the plate boundary. Fig. 9 shows a comparison of dip angles between the Philippine Sea Plate and suggestive interplate earthquakes from the 3-D CMT catalogue. We also compared dip angles of corresponding earthquakes in the F-net MT and GCMT catalogues. Although dip angles of F-net catalogues were higher angles compared to the Philippine Sea Plate, our CMT solutions well correlated with dip angles of the plate boundary. Dip angles of the GCMT catalogue roughly corresponded to dip angles of the Philippine Sea Plate, but our solutions showed better agreements with the plate dip angles. The teleseismic CMT solutions are generally robust, but regional 3-D CMT could provide better constraints of dip angles.

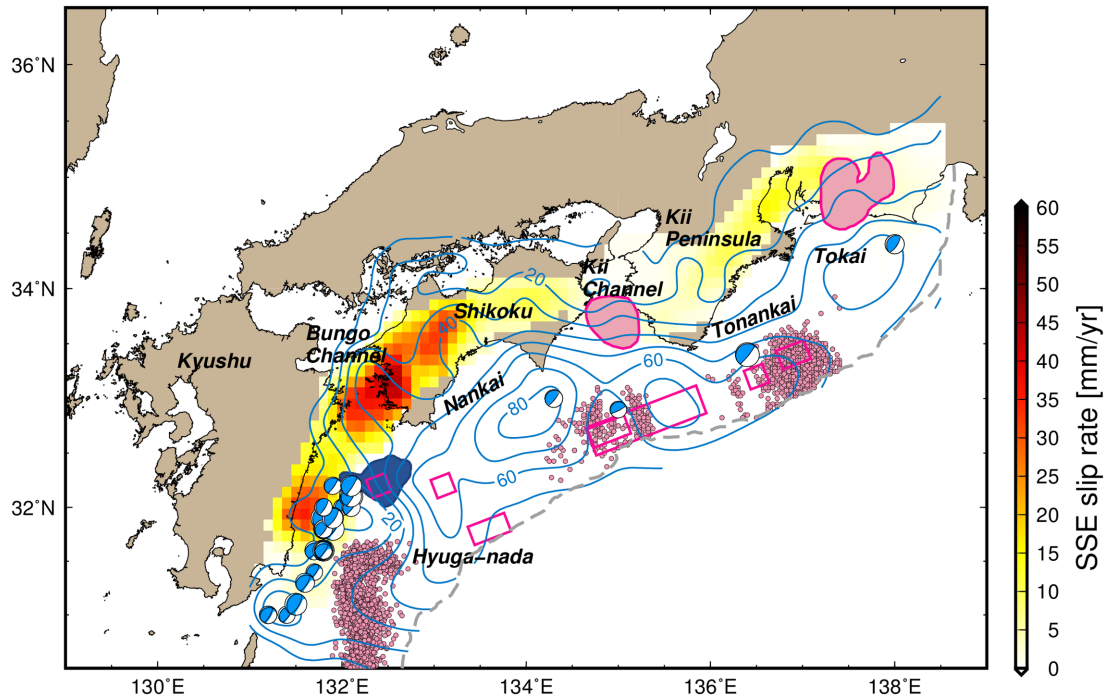


Figure 11. Spatial distribution of slip behaviours on the plate boundary along the Nankai Trough. Plotted focal mechanisms are low-angle thrust faulting solutions at depths around the plate boundary. The coseismic slip area of the 1968 M_w 7.5 Hyuga-nada earthquake (Yagi *et al.* 1998) is shaded in dark blue. SSE slip rates were evaluated from the combined SSE catalogues (Nishimura *et al.* 2013; Takagi *et al.* 2016, 2019). The pink circles indicate the epicentres of the shallow LFTs of the Hyuga-nada and the shallow VLFs in the Tonankai region referred from Yamashita *et al.* (2015) and Takemura, Noda *et al.* (2018). The pink shaded areas and pink rectangles indicate the large slip areas of long-term SSEs (Miyazaki *et al.* 2006, Kobayashi 2014) and shallow SSEs (Yokota & Ishikawa 2020), respectively. The blue contour lines indicate the slip-deficit rates [mm yr^{-1}] on the plate boundary by Noda *et al.* (2018)

We also calculated the VRs between observed and synthetic displacement waveforms to discuss estimation errors of dip angles for offshore earthquakes. Synthetic displacement waveforms were calculated from 3-D Green's functions, assuming double-couple point sources and fixing hypocentre locations and seismic moments. Fig. 10 shows spatial distributions of VRs for the 2016 southeast off Kii Peninsula earthquake and the 2019 Hyuga-nada earthquake. Clear trade-offs between strike and rake angles appeared in the strike-rake plane (upper panels). We confirmed that higher VR values (>75 per cent) only appeared in the regions with dip angles of $5\text{--}15^\circ$ and $10\text{--}20^\circ$ for both earthquakes. Thus, our 3-D CMT provides constraints of dip angles with uncertainties of approximately $\pm 5^\circ$.

4 DISCUSSION

4.1 Slip behaviours on the plate boundary along the Nankai Trough

In order to discuss slip behaviour on the plate boundary, Fig. 11 shows the spatial distribution of slow earthquakes and earthquakes with low-angle ($<25^\circ$) thrust faulting solutions at depths around the plate boundary along the Nankai Trough. The large coseismic slip area of the 1968 M_w 7.5 earthquake (Yagi *et al.* 1998) is indicated by the blue area in Fig. 11. The cumulative deep SSE slips in each grid were determined by summing slip of each SSE in each catalogue (Nishimura *et al.* 2013; Takagi *et al.* 2016, 2019). We then evaluated the SSE slip rates by dividing the cumulative SSE slip at each grid by the analysis period of each catalogue. The SSE slip rate indicates the activity of deep slow earthquakes.

We did not calculate SSE slip rates for shallow SSEs reported by Yokota & Ishikawa (2020) because the number of detected events was still too low at each region. For similar reasons, the long-term SSEs off the Kii Channel (Kobayashi 2014) and Tokai (Miyazaki *et al.* 2006) regions were also excluded from the SSE slip rate calculation. Thus, we plotted the fault configurations or large slip areas of long-term SSEs and shallow SSEs. We also plotted shallow LFTs (Yamashita *et al.* 2015) and shallow VLFs (Takemura *et al.* 2019c) as indicators of shallow slow earthquake activity. The spatial distribution of slip-deficit rates from GNSS and GNSS-A observations by Noda *et al.* (2018), is plotted using blue contour lines in Fig. 11.

At deeper depths (30–40 km), deep slow earthquakes were active, especially in areas with high SSE slip rates, but no interplate regular earthquakes were found. Although SSEs were not removed in the slip-deficit rate estimation of Noda *et al.* (2018)—except for long-term SSEs at the Bungo Channel—the regions with deep SSEs were characterised by low ($20\text{--}40 \text{ mm yr}^{-1}$) slip-deficit rates. At shallower depths ($<30 \text{ km}$) in the offshore region, regular earthquakes, slow earthquakes and high ($>60 \text{ mm yr}^{-1}$) slip-deficit zones were separated from each other. Similar separations of the repeating earthquakes, slow earthquakes, and large coseismic slip areas of megathrust earthquakes at shallower depths were observed in the regions of Tohoku (e.g. Nishikawa *et al.* 2019), Central Ecuador (e.g. Vaca *et al.* 2018) and Costa Rica (e.g. Dixon *et al.* 2014). In particular, Nishikawa *et al.* (2019) pointed out that slow earthquakes were complementarily distributed in the regions surrounding the large coseismic slip area of the 2011 M_w 9.0 Tohoku earthquake. Takemura *et al.* (2019c) pointed out that shallow, slow earthquakes cluster or migrate due to the existence of pore fluid in the transitional regions

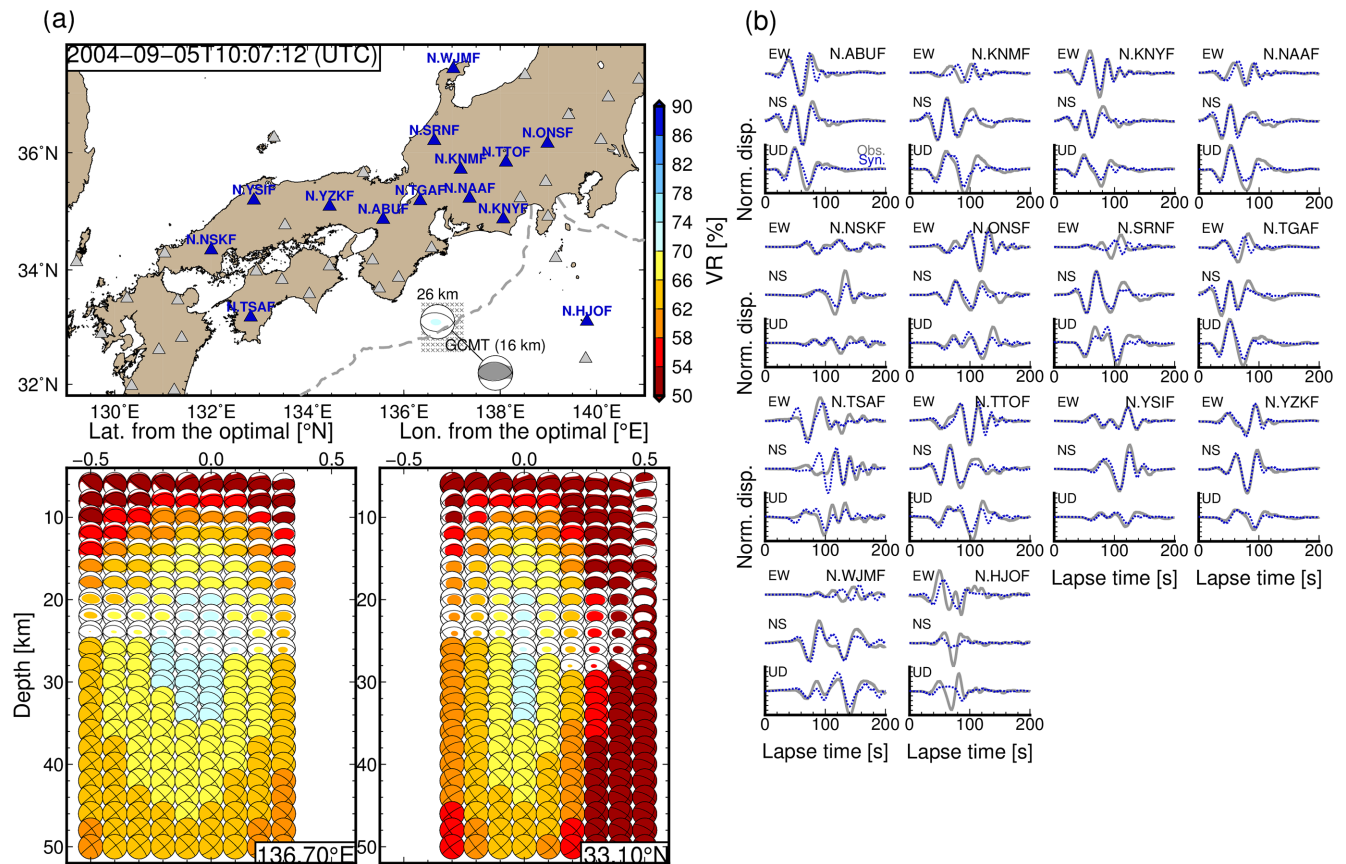


Figure 12. CMT results for the M_w 7.2 southeast off the Kii Peninsula earthquake that occurred on 5 September 2004. Grey focal mechanisms are the solutions of the F-net MT and GCMT catalogues. (a) Locations of the optimal solutions, used stations and depth variations of optimal solutions at each source grid. Colours of the focal mechanisms reflect values of variance reduction between observed and synthetic displacements in the 25–100 s period band. The numbers above the optimal solutions in (a) are the optimal centroid depths. The grey focal mechanism in (a) is the F-net MT solution of this earthquake; (b) Comparisons of observed and synthetic displacements in the 25–100 s period bands. Grey solid and blue dotted lines are the observed and synthetic seismograms, respectively. Synthetic seismograms were evaluated by assuming the optimal solution. Amplitudes at each station were normalized by the maximum amplitude of both observed and synthetic three-component displacement waveforms. Detailed source parameters are listed in Table S2.

between high-strength and low-strength zones of the plate boundary. According to these previous studies and our observations, we suggest that the observed separation between slip behaviours on the plate boundary along the Nankai Trough are related to the heterogeneous distribution of effective strengths on the plate boundary, which is controlled by the frictional coefficient, pore fluid pressure and normal stress.

4.2 Regional 3-D CMT inversions for the M_w 7.2 and 7.5 earthquakes southeast off the Kii Peninsula

We conducted 3-D CMT inversions of offshore earthquakes with M_w of 4.3–6.5. During the analysis period (April 2004 to August 2019), M_w 7.2 and 7.5 intraslab earthquakes occurred southeast off the Kii Peninsula on 5 September 2004. Because typical M_w 7 class earthquakes have rupture durations of 30–50 s and fault areas of 1000–5000 km² (e.g. Kanamori & Brodsky 2004), precise source parameter estimation for such earthquakes is difficult based on our assumptions of the CMT inversion. Despite these disadvantages, the rapid estimation of the CMT solution for these large earthquakes is important for disaster mitigation, such as a CMT-based tsunami warning system. We, therefore, tested our simple CMT inversion for the M_w 7.2 and 7.5 southeast off the Kii Peninsula earthquakes.

Because amplitude saturation of F-net broadband seismometers occurs for regional large earthquakes, we used F-net strong motion seismometers, which have a large clip level and similar frequency response to STS-2 seismometers for periods less than 100 s. We selected F-net stations with distances of 200–500 km from the initial epicentre, which were slightly farther than for the original CMT settings (100–400 km).

Figs 12 and 13 show the results of CMT inversions for the M_w 7.2 and 7.5 earthquakes southeast off the Kii Peninsula, respectively. Detailed estimated parameters are also listed in Table S2. Signal-to-noise ratios were high enough compared to smaller ($M_w < 4.5$) earthquakes in this study but the VRs were low compared to those of moderate earthquakes. The synthetic waveforms roughly corresponded to the observed ones (Figs 12b and 13b). Due to the assumptions of a point source and simple-source time function, detailed characteristics of the observed waveforms were not successfully reproduced. Furthermore, the high (>66 per cent) VR areas were wider than the CMT results for moderate earthquakes within the same region (Fig. 3). The estimated deviatoric components were very similar to those in the GCMT catalogue, but, especially in the result of the M_w 7.2 earthquake, a large isotropic component appeared. Waveform fitting and large non-double couple components suggest the likely complexity of the rupture processes

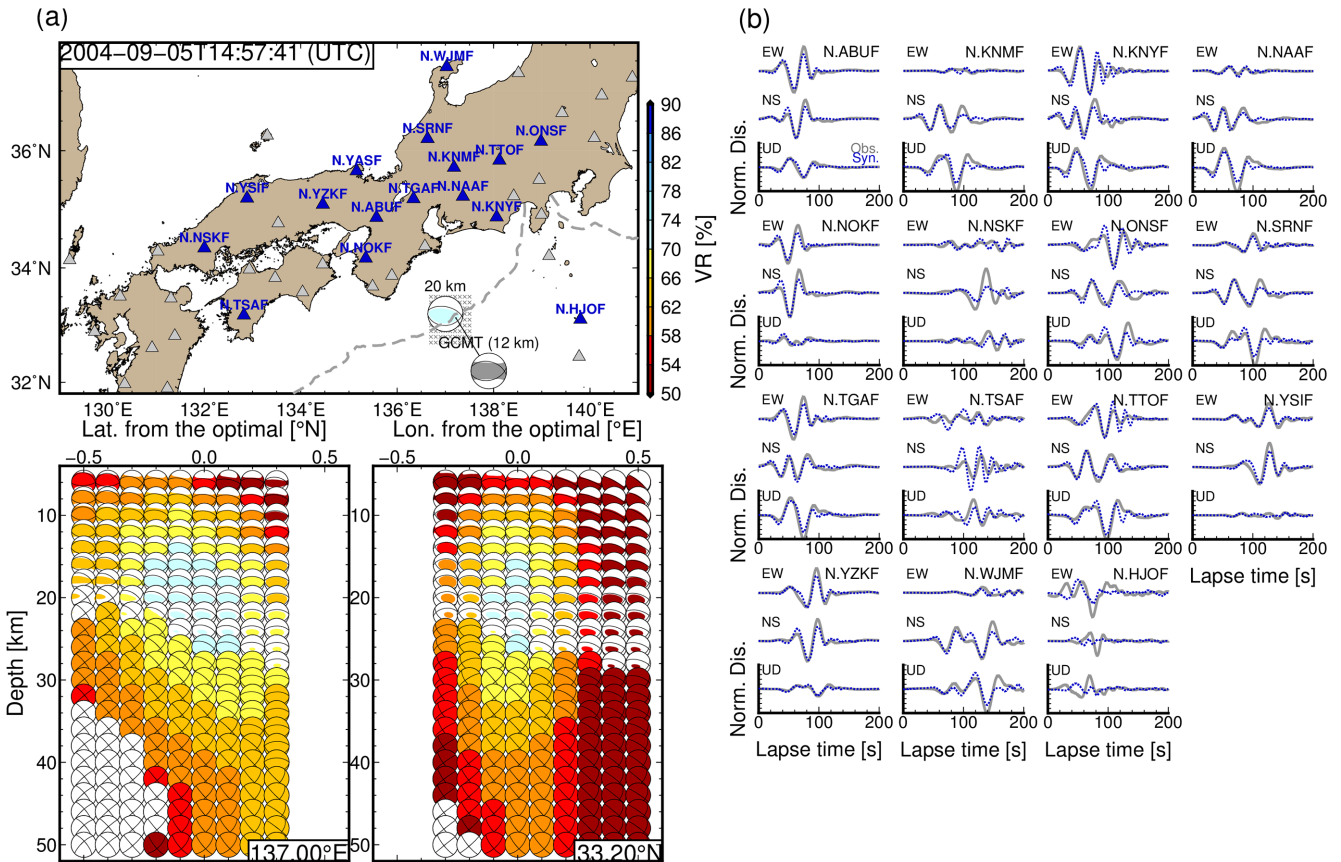


Figure 13. CMT results for the M_w 7.5 southeast off the Kii Peninsula earthquake that occurred on 5 September 2004. (a) Locations of the optimal solutions, used stations and depth variations of optimal solutions at each source grid. Colours of the focal mechanisms reflect values of variance reduction between observed and synthetic displacements in the 25–100 s period bands. The numbers above the optimal solutions in (a) are the optimal centroid depths. The grey focal mechanism in (a) is the F-net MT solution of this earthquake; (b) Comparisons of observed and synthetic displacements in the 25–100 s period band. Grey solid and blue dotted lines are the observed and synthetic seismograms, respectively. Synthetic seismograms were evaluated by assuming the optimal solution. Amplitudes at each station were normalized by the maximum amplitude of both observed and synthetic three-component displacement waveforms. Detailed source parameters are listed in Table S2.

and the source extents for the M_w 7.2 and 7.5 earthquakes. Estimated moment magnitudes were slightly smaller than those of the GCMT catalogue as a result of the analysed period and the deeper centroid depths. Our analysis periods were not significantly larger than the rupture durations of M_w 7 earthquakes, leading to size underestimation. However, the regional 3-D CMT method provides better constraints of dips and depths for offshore earthquakes compared to 1-D CMT systems (Figs 3–6 and 9), and our 3-D grid search required only 15–20 min. These points show the advantages for CMT-based tsunami prediction systems (e.g. Reymond *et al.* 2012; Inazu *et al.* 2016). To obtain more accurate solutions, the CMT method with various durations (e.g. Takemura *et al.* 2019b) or deconvolution method (e.g. Vallée *et al.* 2011) should be implemented. Such sophisticated methods require more time to obtain solutions.

We compared our CMT result for the M_w 7.2 earthquake with the finite-fault model (Okuwaki & Yagi 2018) conducted using teleseismic records based on Yagi & Fukahata (2011). Our horizontal centroid location was very close to an area with large (>3 m) coseismic slips (Fig. 14). The horizontal locations of the dominant slip and centroid locations of the 3-D CMT solution were shared. The centroid location also agreed with that estimated by tsunami record (Satake *et al.* 2005). Thus, we think that the centroid location of the M_w 7.2 earthquake was well constrained by our 3-D CMT

method. The depths of large coseismic slips in the finite fault model ranged from 9 to 18 km, but the optimal centroid depth of the 3-D CMT inversion was 26 km. The depth difference could be due to the regional 3-D heterogeneities (accretionary prism, bathymetry change, and subducting plate). According to the hypocentre determinations derived using ocean-bottom seismometers (Sakai *et al.* 2005; Nakano *et al.* 2015), the hypocentres of aftershocks due to the M_w 7.5 earthquake were distributed at depths of approximately 10–30 km. We also tested the centroid depth and large isotropic components by our 3-D CMT inversion. By using simulated seismograms of the finite-fault model (Okuwaki & Yagi 2018) as observed seismograms, we conducted CMT inversion of the simulated M_w 7.2 intraslab earthquake (Fig. S6). The centroid location and depth well corresponded to the large slip area of the finite-fault model. The large isotropic component was also estimated. Thus, large non-double couple components suggest the likely complexity of the rupture processes and the source extents for the finite-fault model of the M_w 7.2 earthquake. Based on the hypocentre distribution of aftershocks, the fault dimensions of the M_w 7.2 earthquake and synthetic test, we considered that the extension of seismic slips at depths of approximately 26 km might be possible.

The detailed rupture processes of the M_w 7.2 and 7.5 earthquakes remain unclear. The regional seismic data and 3-D Green's functions may provide additional constraints for large offshore earthquakes.

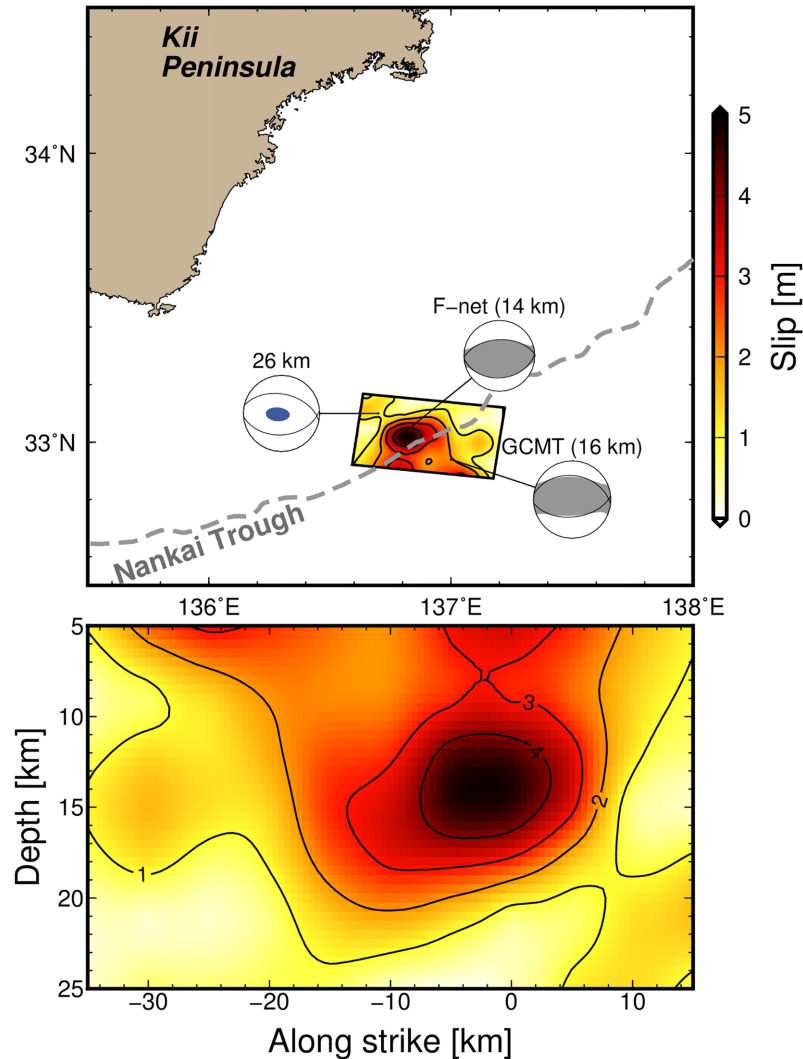


Figure 14. Comparison of the CMT results for the M_w 7.2 southeast off the Kii Peninsula earthquake and other CMT catalogues (Fukuyama *et al.* 1998; Kubo *et al.* 2002; Ekström *et al.* 2012) and finite fault modelling (Okuwaki and Yagi 2018) solutions. The bottom panel is the slip distribution of the finite fault model in the strike-depth plane.

The finite fault modelling based on the 3-D Green's functions is an important but challenging issue that requires particular attention in future studies.

5 CONCLUSION

We conducted 3-D CMT inversions of moderate earthquakes along the Nankai Trough using the regional 3-D Green's function data set. By comparing 3-D CMT solutions with those in the F-net catalogue, large differences in focal mechanisms and centroid depths were found for offshore earthquakes. These differences could be caused by 3-D offshore heterogeneities, such as the low-velocity accretionary prism and subducting Philippine Sea plate. Onshore MT inversion using a simple 1-D earth model could provide incorrect estimations due to offshore heterogeneities and station coverage. By introducing the effects of such 3-D heterogeneities, the 3-D CMT solutions for offshore earthquakes practically agreed with hypocentre distributions determined by ocean-bottom seismometers. Furthermore, our CMT method based on onshore seismograms provided better constrained focal mechanisms and centroid depths compared

to the F-net MT catalogue. We also compared our CMT solutions with those of the GCMT catalogue. The teleseismic CMT solutions are generally robust but regional 3-D CMT could provide better constraints of dip angles. The regional 3-D CMT catalogue contains more earthquakes compared to the GCMT catalogue, where only earthquakes with about $M_w > 5$ are listed. To investigate detailed decade-scale seismicity in a certain region, CMT inversion incorporating regional 3-D velocity model should be required.

Although no suggestive interplate earthquakes are listed in the 1-D catalogue, some low-angle thrust faulting solutions at depths around the plate boundary were confirmed by our 3-D CMT catalogue. These earthquakes could be interpreted as interplate earthquakes. By using our 3-D CMT catalogue and previously published slow earthquake models, we illustrated the spatial distribution of slip behaviours on the plate boundary along the Nankai Trough. Regular interplate earthquakes and slow earthquakes occur within different segments on the plate boundary. These separated distributions might reflect the heterogeneous distribution of effective strength on the plate boundary. The gap zones, where no regular interplate and slow earthquakes occurred, were found in the Nankai, Tonankai and Tokai regions. These were the regions with large

(>60 mm yr⁻¹) slip-deficit rates, where the plate boundary can be strongly coupled.

The regional CMT inversion of earthquakes with $M_w > 7$ was generally difficult due to their fault size and the amplitude saturation of the broadband sensors. CMT inversions for the 2004 M_w 7.2 and 7.5 intraslab earthquakes southeast of the Kii Peninsula were performed using the regional broadband strong motion sensors of F-net. Although signal-to-noise ratios of the observed displacements were good enough, the waveform fittings of the M_w 7.2 and 7.5 intraslab earthquakes were not good compared to those of typical moderate earthquakes due to fault sizes and the rupture complexity. However, the centroid location agreed with that estimated by tsunami record, and the focal mechanism could be constrained. These points and the rapid availability of a solution could be the advantages for CMT-based tsunami warning systems.

ACKNOWLEDGEMENTS

F-net waveform data and the F-net MT catalogue are available via the website of the National Research Institute for Earth Science and Disaster Resilience (<https://doi.org/10.17598/NIED.0005>). Bathymetric depth data were obtained from ETOPO1 (Amante and Eakins 2009). OpenSWPC software (Maeda *et al.* 2017) and the 3-D model of Koketsu *et al.* (2012) were obtained from <https://github.com/takuto-maeda/OpenSWPC> and https://www.jishin.go.jp/evaluation/seismic_hazard_map/lpshm/12_choshuki_dat/, respectively. Generic Mapping Tools (Wessel *et al.* 2013) and Seismic Analysis Code (SAC; Helffrich *et al.* 2013) were used to make the figures and when conducting the signal processing work, respectively. The catalogue of slow earthquakes (Nishimura *et al.* 2013; Yamashita *et al.* 2015; Takagi *et al.* 2016) was downloaded from the Slow Earthquake Database website (Kano *et al.* 2018; <http://www-solid.eps.s.u-tokyo.ac.jp/~sloweq/>). Our CMT catalogue and CMT results of assumed source grids for each earthquake are available from <https://doi.org/10.5281/zenodo.3674161>. The FDM simulations of seismic wave propagation were conducted on the computer system of the Earthquake and Volcano Information Center at the Earthquake Research Institute, the University of Tokyo. This study was supported by the Japan Society for the Promotion of Science (JSPS) KAKENHI Grant Numbers 17K14382 under the Grant-in-Aid for Young Scientists (B) and 19H04626 under Scientific Research under Innovative Areas ‘Science of Slow Earthquakes’. We also thank Dr J. Braunmiller, an anonymous reviewer and Editor Prof J. Virieux for careful reviewing and constructive comments, which have helped to improve the manuscript.

REFERENCES

Aki, K. & Richards, P., 2002. *Quantitative Seismology*, 2nd ed., University Science Books. Retrieved from https://www.ideo.columbia.edu/~richards/Aki_Richards.html.

Amante, C. & Eakins, B.W., 2009. ETOPO1 1 arc-minute global relief model: Precedures, data sources and analysis, NOAA Technical Memorandum NESDIS NGDC-24, Natl. Geophys. Data Center, NOAA, 19 pp., doi:10.7289/V5C8276M.

Ando, M., 1975. Source mechanisms and tectonic significance of historical earthquakes along the Nankai trough, Japan. *Tectonophysics*, **27**, 119–140.

Dixon, T.H., Jiang, Y., Malservisi, R., McCaffrey, R., Voss, N., Protti, M. & Gonzalez, V., 2014. Earthquake and tsunami forecasts: relation of slow slip events to subsequent earthquake rupture. *Proc. Natl. Acad. Sci.*, **111**, 17039–17044.

Dziewonski, A.M., Chou, T.-A. & Woodhouse, J.H., 1981. Determination of earthquake source parameters from waveform data for studies of global and regional seismicity. *J. geophys. Res.*, **86**, 2825–2852.

Eberhart-Phillips, D., Reyners, M., Bannister, S., Chadwick, M. & Ellis, S., 2010. Establishing a versatile 3-D seismic velocity model for New Zealand. *Seismol. Res. Lett.*, **81**, 992–1000.

Eisner, L. & Clayton, R.W., 2001. A reciprocity method for multiple-source simulations. *Bull. seism. Soc. Am.*, **91**, 553–560.

Ekström, G., Nettles, M. & Dziewoński, A.M., 2012. The global CMT project 2004–2010: centroid-moment tensors for 13,017 earthquakes. *Phys. Earth planet. Inter.*, **200–201**, 1–9.

Fukuyama, E., Ishida, M., Dreger, D.S. & Kawai, H., 1998. Automated seismic moment tensor determination by using on-line broadband seismic waveforms. *Zisin*, **51**, 149–156.

Gokhberg, A. & Fichtner, A., 2016. Full-waveform inversion on heterogeneous HPC systems. *Comput. Geosci.*, **89**, 260–268.

Gomberg, J., 2018. Cascadia onshore-offshore site response, submarine sediment mobilization, and earthquake recurrence. *J. geophys. Res.*, **123**, 1381–1404.

Hardebeck, J.L. & Shearer, P.M., 2002. A new method for determining first-motion focal mechanisms. *Bull. seism. Soc. Am.*, **92**, 2264–2276.

Hejrani, B., Tkalčić, H. & Fichtner, A., 2017. Centroid moment tensor catalogue using a 3-D continental scale Earth model: application to earthquakes in Papua New Guinea and the Solomon Islands. *J. geophys. Res.*, **122**, 5517–5543.

Helffrich, G., Woakey, J. & Bastow, I., 2013. *The Seismic Analysis Code*, Cambridge Univ. Press. doi:10.1017/CBO9781139547260.

Helffrich, G.R., 1997. How good are routinely determined focal mechanisms? Empirical statistics based on a comparison of Harvard, USGS and ERI moment tensors. *Geophys. J. Int.*, **131**, 741–750.

Hirose, F., Nakajima, J. & Hasegawa, A., 2008. Three-dimensional seismic velocity structure and configuration of the Philippine Sea slab in south-western Japan estimated by double-difference tomography. *J. geophys. Res.*, **113**, 1–26.

Inazu, D., Pulido, N., Fukuyama, E., Saito, T., Senda, J. & Kumagai, H., 2016. Near-field tsunami forecast system based on near real-time seismic moment tensor estimation in the regions of Indonesia, the Philippines, and Chile 4. *Seismology. Earth, Planets Space*, **68**, doi:10.1186/s40623-016-0445-x.

Ito, Y. & Obara, K., 2006. Dynamic deformation of the accretionary prism excites very low frequency earthquakes. *Geophys. Res. Lett.*, **33**, L02311.

Kamei, R., Pratt, R.G. & Tsuji, T., 2012. Waveform tomography imaging of a megasplay fault system in the seismogenic Nankai subduction zone. *Earth planet. Sci. Lett.*, **317–318**, 343–353.

Kanamori, H. & Brodsky, E.E., 2004. The physics of earthquakes. *Rep. Prog. Phys.*, **67**, 1429–1496.

Kanamori, H. & Rivera, L., 2008. Source inversion of W phase: speeding up seismic tsunami warning. *Geophys. J. Int.*, **175**, 222–238.

Kaneko, Y. *et al.*, 2019. Ultra-long duration of seismic ground motion arising from a thick, low-velocity sedimentary wedge. *J. geophys. Res.*, **124**, 10 347–10 359.

Kano, M. *et al.*, 2018. Development of a slow earthquake database. *Seismol. Res. Lett.*, **89**, 1566–1575.

Kikuchi, M. & Kanamori, H., 1991. Inversion of complex body waves-III. *Bull. seism. Soc. Am.*, **81**, 2335–2350.

Kimura, T., Murakami, H. & Matsumoto, T., 2015. Systematic monitoring of instrumentation health in high-density broadband seismic networks. *Earth, Planets Space*, **67**, 55.

Kobayashi, A., 2014. A long-term slow slip event from 1996 to 1997 in the Kii Channel, Japan. *Earth, Planets Space*, **66**, 1–7.

Koketsu, K., Miyake, H. & Suzuki, H., 2012. Japan integrated velocity structure model version 1, in *Proceedings of the 15th World Conf. Earthq. Eng.*, pp. 1–4. Retrieved from <http://www.iitk.ac.in/nicee/wcee/article/WCEE2012.1773.pdf>.

Kubo, A., Fukuyama, E., Kawai, H. & Nonomura, K., 2002. NIED seismic moment tensor catalogue for regional earthquakes around Japan: quality test and application. *Tectonophysics*, **356**, 23–48.

- Kubota, T., Suzuki, W., Nakamura, T., Chikada, N.Y., Aoi, S., Takahashi, N. & Hino, R., 2018. Tsunami source inversion using time-derivative waveform of offshore pressure records to reduce effects of non-tsunami components. *Geophys. J. Int.*, **215**, 1200–1214.
- Kuge, K. & Kawakatsu, H., 1993. Significance of non-double couple components of deep and intermediate-depth earthquakes: implications from moment tensor inversions of long-period seismic waves. *Phys. Earth planet. Inter.*, **75**, 243–266.
- Lee, S.-J. et al., 2013. Towards real-time regional earthquake simulation I: real-time moment tensor monitoring (RMT) for regional events in Taiwan. *Geophys. J. Int.*, **196**, 432–446.
- Maeda, T., Takemura, S. & Furumura, T., 2017. OpenSWPC: an open-source integrated parallel simulation code for modeling seismic wave propagation in 3D heterogeneous viscoelastic media. *Earth, Planets Space*, **69**, 102.
- Miyazaki, S., Segall, P., McGuire, J.J., Kato, T. & Hatanaka, Y., 2006. Spatial and temporal evolution of stress and slip rate during the 2000 Tokai slow earthquake. *J. geophys. Res.*, **111**, 1–17.
- Nakanishi, A., Kodaira, S., Park, J.-O. & Kaneda, Y., 2002. Deformable backstop as seaward end of coseismic slip in the Nankai Trough seismogenic zone. *Earth planet. Sci. Lett.*, **203**, 255–263.
- Nakano, M., Nakamura, T. & Kaneda, Y., 2015. Hypocenters in the Nankai Trough determined by using data from both ocean-bottom and land seismic networks and a 3D velocity structure model: implications for seismotectonic activity. *Bull. seism. Soc. Am.*, **105**, 1594–1605.
- Nakano, M. et al., 2018a. The 2016 Mw 5.9 earthquake off the southeastern coast of Mie Prefecture as an indicator of preparatory processes of the next Nankai Trough megathrust earthquake. *Prog. Earth Planet. Sci.*, **5**, 30.
- Nakano, M., Hori, T., Araki, E., Kodaira, S. & Ide, S., 2018b. Shallow very-low-frequency earthquakes accompany slow slip events in the Nankai subduction zone. *Nat. Commun.*, **9**, 984.
- National Research Institute for Earth Science and Disaster Resilience, 2019. NIED F-net. Natl. Res. Inst. Earth Sci. Disaster Resil, doi:10.17598/NIED.0005.
- Nishikawa, T., Matsuzawa, T., Ohta, K., Uchida, N., Nishimura, T. & Ide, S., 2019. The slow earthquake spectrum in the Japan Trench illuminated by the S-net seafloor observatories. *Science*, **365**, 808–813.
- Nishimura, T., Matsuzawa, T. & Obara, K., 2013. Detection of short-term slow slip events along the Nankai Trough, southwest Japan, using GNSS data. *J. geophys. Res.*, **118**, 3112–3125.
- Noda, A., Saito, T. & Fukuyama, E., 2018. Slip-deficit rate distribution along the Nankai Trough, Southwest Japan, with elastic lithosphere and viscoelastic asthenosphere. *J. geophys. Res.*, **123**, 8125–8142.
- Okada, Y., Kasahara, K., Hori, S., Obara, K., Sekiguchi, S., Fujiwara, H. & Yamamoto, A., 2004. Recent progress of seismic observation networks in Japan—Hi-net, F-net, K-NET and KiK-net. *Earth, Planets Space*, **56**, xv–xxviii.
- Okamoto, T., Takenaka, H. & Nakamura, T., 2018. Evaluation of accuracy of synthetic waveforms for subduction-zone earthquakes by using a land–ocean unified 3D structure model. *Earth, Planets Space*, **70**, doi:10.1186/s40623-018-0871-z.
- Okuwaki, R. & Yagi, Y., 2018. Seismic source model for the Mw 7.2 2004 Kii peninsula, Japan, earthquake. *GitHub*. doi:10.5281/zenodo.1493833.
- Park, J.-O. et al., 2010. A low-velocity zone with weak reflectivity along the Nankai subduction zone. *Geology*, **38**, 283–286.
- Ramos-Martínez, J. & McMechan, G.A., 2001. Source-parameter estimation by full waveform inversion in 3D heterogeneous, viscoelastic, anisotropic media. *Bull. seism. Soc. Am.*, **91**, 276–291.
- Reymond, D., Okal, E.A., Hébert, H. & Bourdet, M., 2012. Rapid forecast of tsunami wave heights from a database of pre-computed simulations, and application during the 2011 Tohoku tsunami in French Polynesia. *Geophys. Res. Lett.*, **39**, 1–6.
- Saito, T., Noda, A., Yoshida, K. & Tanaka, S., 2018. Shear strain energy change caused by the interplate coupling along the Nankai Trough: an integration analysis using stress tensor inversion and slip deficit inversion. *J. geophys. Res.*, **123**, 5975–5986.
- Sakai, S. et al., 2005. Urgent aftershock observation of the 2004 off the Kii Peninsula earthquake using ocean bottom seismometers. *Earth Planets Space*, **57**, 363–368.
- Satake, K. et al., 2005. Tsunami source of the 2004 off the Kii Peninsula earthquakes inferred from offshore tsunami and coastal tide gauges. *Earth, Planets Space*, **57**, 173–178.
- Shapiro, N.M., Campillo, M., Singh, S.K. & Pacheco, J., 1998. Seismic channel waves in the accretionary prism of the Middle America Trench. *Geophys. Res. Lett.*, **25**, 101–104.
- Shelly, D.R., Hardebeck, J.L., Ellsworth, W.L. & Hill, D.P., 2016. A new strategy for earthquake focal mechanisms using waveform-correlation-derived relative polarities and cluster analysis: application to the 2014 Long Valley Caldera earthquake swarm. *J. geophys. Res.*, **121**, 8622–8641.
- Shiomi, K., Obara, K. & Sato, H., 2006. Moho depth variation beneath southwestern Japan revealed from the velocity structure based on receiver function inversion. *Tectonophysics*, **420**, 205–221.
- Storchak, D.A., Giacomo, D. Di, Bondár, I., Engdahl, E.R., Harris, J., Lee, W.H.K. & Villaseñor, A., 2013. Public Release of the ISC – GEM Global Instrumental Earthquake Catalogue, 1900–2009). *Seismol. Res. Lett.*, **84**, 810–815.
- Tahara, M. et al., 2008. Seismic velocity structure around the Hyuganada region, Southwest Japan, derived from seismic tomography using land and OBS data and its implications for interplate coupling and vertical crustal uplift. *Phys. Earth planet. Inter.*, **167**, 19–33.
- Takagi, R., Obara, K. & Maeda, T., 2016. Slow slip event within a gap between tremor and locked zones in the Nankai subduction zone. *Geophys. Res. Lett.*, **43**, 1066–1074.
- Takagi, R., Uchida, N. & Obara, K., 2019. Along-strike variation and migration of long-term slow slip events in the Western Nankai subduction zone, Japan. *J. geophys. Res.*, **124**, 3853–3880.
- Takemura, S., Shiomi, K., Kimura, T. & Saito, T., 2016. Systematic difference between first—motion and waveform—inversion solutions for shallow offshore earthquakes due to a low - angle dipping slab. *Earth, Planets Space*, 1–8, doi:10.1186/s40623-016-0527-9.
- Takemura, S., Kimura, T., Saito, T., Kubo, H. & Shiomi, K., 2018a. Moment tensor inversion of the 2016 southeast offshore Mie earthquake in the Tonankai region using a three-dimensional velocity structure model: effects of the accretionary prism and subducting oceanic plate. *Earth, Planets Space*, **70**, 50, doi:10.1186/s40623-018-0819-3.
- Takemura, S., Matsuzawa, T., Kimura, T., Tonegawa, T. & Shiomi, K., 2018b. Centroid moment tensor inversion of shallow very low frequency earthquakes off the Kii Peninsula, Japan, using a three-dimensional velocity structure model. *Geophys. Res. Lett.*, **45**, 6450–6458.
- Takemura, S., Kubo, H., Tonegawa, T., Saito, T. & Shiomi, K., 2019a. Modeling of Long-Period Ground Motions in the Nankai Subduction Zone: Model Simulation Using the Accretionary Prism Derived from Oceanfloor Local S-Wave Velocity Structures. *Pure appl. Geophys.*, **176**, 627–647.
- Takemura, S., Matsuzawa, T., Noda, A., Tonegawa, T., Asano, Y., Kimura, T. & Shiomi, K., 2019b. Structural characteristics of the Nankai trough shallow plate boundary inferred from shallow very low frequency earthquakes. *Geophys. Res. Lett.*, **46**, 4192–4201.
- Takemura, S., Noda, A., Kubota, T., Asano, Y., Matsuzawa, T. & Shiomi, K., 2019c. Migrations and Clusters of Shallow Very Low Frequency Earthquakes in the Regions Surrounding Shear Stress Accumulation Peaks Along the Nankai Trough. *Geophys. Res. Lett.*, **46**, 11 830–11 840.
- Terakawa, T. & Matsu'ura, M., 2010. The 3-D tectonic stress fields in and around Japan inverted from centroid moment tensor data of seismic events. *Tectonics*, **29**, 1–14.
- Townend, J. & Zoback, M.D., 2006. Stress, strain, and mountain building in central Japan. *J. geophys. Res.*, **111**, 1–11.
- Vaca, S., Vallée, M., Nocquet, J.M., Battaglia, J. & Régnier, M., 2018. Recurrent slow slip events as a barrier to the northward rupture propagation of the 2016 Pedernales earthquake (Central Ecuador). *Tectonophysics*, **724–725**, 80–92.
- Vallée, M., Charléty, J., Ferreira, A.M.G., Delouis, B. & Vergoz, J., 2011. SCARDEC: A new technique for the rapid determination of seismic

- moment magnitude, focal mechanism and source time functions for large earthquakes using body-wave deconvolution. *Geophys. J. Int.*, **184**, 338–358.
- Wallace, L.M. *et al.*, 2016. Near-field observations of an offshore M w 6.0 earthquake from an integrated seafloor and subseafloor monitoring network at the Nankai Trough, southwest Japan. *J. geophys. Res.*, **121**, 8338–8351.
- Wang, X. & Zhan, Z., 2020. Moving from 1-D to 3-D velocity model: automated waveform-based earthquake moment tensor inversion in the Los Angeles region. *Geophys. J. Int.*, **220**, 218–234.
- Wessel, P., Smith, W.H.F., Scharroo, R., Luis, J. & Wobbe, F., 2013. Generic mapping tools: improved version released. *EOS, Trans. Am. geophys. Un. (Washington. DC)*, **94**, 409–410.
- Yagi, Y., Kikuchi, M., Yoshida, S. & Yamanaka, Y., 1998. Source process of the Hyuga-nada earthquake of April 1, 1968 (MJMA 7.5), and its relationship to the subsequent seismicity. *Zisin (J. Seismol. Soc. Japan. 2nd ser.)*, **51**, 139–148.
- Yagi, Y. & Fukahata, Y., 2011. Introduction of uncertainty of Green's function into waveform inversion for seismic source processes. *Geophys. J. Int.*, **186**, 711–720.
- Yamashita, Y., Shimizu, H. & Goto, K., 2012. Small repeating earthquake activity, interplate quasi-static slip, and interplate coupling in the Hyuga-nada, southwestern Japan subduction zone. *Geophys. Res. Lett.*, **39**, 1–5.
- Yamashita, Y. *et al.*, 2015. Migrating tremor off southern Kyushu as evidence for slow slip of a shallow subduction interface. *Science*, **348**, 676–679.
- Yokota, Y. & Ishikawa, T., 2020. Shallow slow slip events along the Nankai Trough detected by GNSS-A. *Sci. Adv.*, **6**, doi:10.1126/sciadv.aay5786.

SUPPORTING INFORMATION

Supplementary data are available at *GJI* online.

2019TakemuraOkuwakiKubotaShiomiKimuraNoda_SM.pdf

Please note: Oxford University Press is not responsible for the content or functionality of any supporting materials supplied by the authors. Any queries (other than missing material) should be directed to the corresponding author for the paper.